The Astrophysical Journal, 882:168 (16pp), 2019 September 10 https://doi.org/10.3847/1538-4357/ab3a46

Low Star Formation Efficiency in Typical Galaxies at $z = 5$–6

Riccardo Pavesi[1], Dominik A. Riechers[1,2], Andreas L. Faisst[3], Gordon J. Stacey[1], and Peter L. Capak[3]
[1] Department of Astronomy, Cornell University, Space Sciences Building, Ithaca, NY 14853, USA; rp462@cornell.edu
[2] Max Planck Institute for Astronomy, Königstuhl 17, D-69117 Heidelberg, Germany
[3] Infrared Processing and Analysis Center, California Institute of Technology, Pasadena, CA 91125, USA
Received 2018 November 30; revised 2019 July 29; accepted 2019 August 8; published 2019 September 16

Abstract

Using the Very Large Array and ALMA, we have obtained CO(2–1), [C II], and [N II] line emission and multiple dust continuum measurements in a sample of "normal" galaxies at $z = 5$–6. We report the highest-redshift detection of low-J CO emission from a Lyman break galaxy, at $z \sim 5.7$. The CO line luminosity implies a massive molecular gas reservoir of $(1.3 \pm 0.3)(\alpha_{\rm CO}/4.5\,M_\odot\,({\rm K\,km\,s^{-1}\,pc^2})^{-1}) \times 10^{11}\,M_\odot$, suggesting low star formation efficiency with a gas depletion timescale of order ∼1 Gyr. This efficiency is much lower than traditionally observed in $z \gtrsim 5$ starbursts, indicating that star-forming conditions in main-sequence galaxies at $z \sim 6$ may be comparable to those of normal galaxies probed up to $z \sim 3$ to date but with rising gas fractions across the entire redshift range. We also obtain a deep CO upper limit for a main-sequence galaxy at $z \sim 5.3$ with an approximately three times lower star formation rate, perhaps implying a high $\alpha_{\rm CO}$ conversion factor, as typically found in low-metallicity galaxies. For a sample including both CO targets, we also find faint [N II] 205 μm emission relative to [C II] in all but the most IR-luminous "normal" galaxies at $z = 5$–6, implying more intense or harder radiation fields in the ionized gas relative to lower redshift. These radiation properties suggest that low metallicity may be common in typical $\sim 10^{10}\,M_\odot$ galaxies at $z = 5$–6. While a fraction of main-sequence star formation in the first billion yr may take place in conditions not dissimilar to lower redshift, lower metallicity may affect the remainder of the population.

Key words: cosmology: observations – galaxies: formation – galaxies: high-redshift – galaxies: ISM – galaxies: star formation – radio lines: galaxies

1. Introduction

Massive galaxies started forming during the epoch of reionization at $z > 6$ and may have experienced their fastest growth toward the end of the first billion yr of cosmic time ($z \sim 4$–6), doubling their stellar mass content on timescales of order of 100 million yr (e.g., Bouwens et al. 2015; Faisst et al. 2016a). While the high-redshift universe offers the promise of strong new constraints to dark matter physics through early halo growth (e.g., Buckley & Peter 2018), they have, so far, been limited to coarse stellar mass–halo mass relationships that do not capture the variety in galaxy formation history hinted at by observations (e.g., Behroozi et al. 2019; Moster et al. 2018; Tacchella et al. 2018). The details of such an early growth epoch at $z > 5$ may also carry the imprint of cosmic reionization, therefore shining light on the physics of the dark ages (e.g., Ferrara 2016; Castellano et al. 2018; Ma et al. 2018).

Crucially, while abundant optical and near-infrared (NIR) observations have revealed the end product of early galaxy formation (e.g., Bouwens et al. 2015), the drivers of such evolution are the gas processes of intense gas inflows, outflows, and cooling that lead to primordial star formation, galaxy growth, and dynamical assembly (e.g., Davé et al. 2011; Hopkins et al. 2014). Such gas flows are difficult to observe directly, but measurements of the gas conditions provide the most direct constraints on the physics of early galaxy evolution. For example, the observable gas-phase metallicity probes the balance between gas inflows, outflows, and metal enrichment due to star formation (e.g., Tremonti et al. 2004; Davé et al. 2012; Lilly et al. 2013). On the other hand, the relationship between local gas properties and star formation rate (SFR; the "star formation law") in early, forming galaxies provides the critical link between observable stellar properties and the more fundamental properties of the interstellar gas (e.g., Krumholz et al. 2018; Sharda et al. 2018). Since the "star formation law" may emerge from the complex effects of stellar feedback and local gas dynamics, it is of great interest to explore its redshift evolution and any variations across galaxy types and gas conditions (e.g., Daddi et al. 2010b; Genzel et al. 2015; Scoville et al. 2016, 2017; Orr et al. 2018; Tacconi et al. 2018). A promising way to better constrain the gas metallicity and star formation law in "normal" galaxies is to utilize tracers of the stat-forming gas phase. In this work, we take advantage of the latest radio and (sub)millimeter interferometers to probe such tracers up to the first billion yr of cosmic time.

The CO rotational transitions and atomic fine structure lines in the far-infrared (FIR) provide some of the most accurate tracers of the properties of the star-forming interstellar medium (ISM) in galaxies because they are bright, unaffected by dust extinction, and probe all of the main gas phases (e.g., Stacey et al. 1991; Hollenbach & Tielens 1997; Kaufman et al. 1999; Carilli & Walter 2013). In order to constrain the star formation law, we need to trace the cold molecular gas mass, because it is found to be most causally connected to star formation in local galaxies (Bigiel et al. 2011; Schruba et al. 2011; Carilli & Walter 2013; Leroy et al. 2013). The best-characterized tracers of such molecular gas are the low-J rotational emission lines of the CO molecule, which have been calibrated within the Milky Way and in local galaxies and achieve a high degree of consistency (e.g., Leroy et al. 2011; Bolatto et al. 2013; Sandstrom et al. 2013). These measurements may depend on metallicity estimates, since metallicity appears to strongly affect the fraction of molecular gas-emitting CO lines and, therefore, the gas mass-to-light ratio $\alpha_{\rm CO}$ (e.g., Maloney & Black 1988; Madden et al. 1997; Kaufman et al. 1999;

Bolatto et al. 2013). However, it is difficult to measure metallicity directly in the cold molecular medium because no hydrogen lines are directly accessible. Indirect tracers of metallicity typically involve either probes of the nitrogen abundance ratio to other metals or probes of the hardness and intensity of the radiation field (e.g., Masters et al. 2016; Vincenzo et al. 2016). The latter technique rests on observations of local dwarf galaxies, which have shown that lower-metallicity environments may produce harder and more intense ultraviolet radiation, producing stronger lines from higher ionization states (e.g., Cormier et al. 2015; Croxall et al. 2017). Therefore, joint measurements of CO and of metallicity probes for the same sample are of key interest to relate high-redshift observations to the mechanisms that have been investigated and understood at low redshift.

The [C II] line at 158 μm is now commonly observed at high redshift as a probe of the star-forming gas and the gas dynamics in star-forming galaxies due to its widespread distribution (e.g., Stacey et al. 1991, 2010; Maiolino et al. 2005, 2009; Walter et al. 2009; Riechers et al. 2013, 2014). The [C II]/IR luminosity ratio appears to trace the surface density of star formation, providing an important measure of starburstiness (e.g., Luhman et al. 1998; Malhotra et al. 2001). Crucially, metallicity was shown to be the primary variable controlling the residual scatter in the [C II]/IR–$\Sigma_{\rm IR}$ relation (Smith et al. 2017). However, the [C II] line can originate from gas where hydrogen is ionized, neutral, or molecular. Therefore, observations of additional diagnostic lines that probe specific phases of the ISM are required to connect observations to physical conditions. In particular, the [N II] line at 205 μm is expected to be emitted under similar conditions of radiation intensity and gas density to [C II] but uniquely from the ionized phase (e.g., Oberst et al. 2006; Decarli et al. 2014; Pavesi et al. 2016; Díaz-Santos et al. 2017), thereby assessing the fraction of [C II] coming from ionized rather than neutral gas. The [C II]/[N II] line ratio has been proposed as a metallicity tracer due to its sensitivity to abundance ratios (Nagao et al. 2011, 2012), especially the hardness of the radiation field as traced by the ionization state of carbon and nitrogen in the ionized gas (Cormier et al. 2015; Pavesi et al. 2016). Croxall et al. (2017) conclusively demonstrated a strong correlation between gas-phase metallicity and the [C II]/[N II] line ratio using a sample of local galaxies.

Few direct observations of the ISM in galaxies at $z > 5$ are available, and the most luminous galaxies have almost exclusively been targeted to date, in particular quasar hosts and the brightest dusty star-forming galaxies (DSFGs; Maiolino et al. 2005, 2009; Walter et al. 2009, 2012; Riechers et al. 2013, 2014; Gullberg et al. 2015; Strandet et al. 2017). Although their brightness allows a great level of detail (e.g., Riechers et al. 2013), it is unlikely that the conditions in the most extreme outliers are representative of typical galaxies. For example, although the fraction of dust-obscured star formation in extreme starbursts is close to unity, and their metallicity may be close to solar (e.g., Magdis et al. 2011), the first ALMA sample study of [C II] at 158 μm and dust emission from normal galaxies at $z > 5$ found lower dust emission than expected (Riechers et al. 2014; Capak et al. 2015; Barišić et al. 2017; Faisst et al. 2017). We have conducted these studies of galaxies in the parent sample, which is constituted of "typical" (i.e., $\sim L^{*}_{\rm UV}$) galaxies with $M_{*} \sim 10^{10} M_{\odot}$ selected from a representative spectroscopic sample containing galaxies in various evolutionary stages selected as Lyman break galaxies (LBGs) or Lyman alpha emitters (LAEs; i.e., the two most common selection techniques at $z > 5$). Since the ultraviolet luminosity of these galaxies is near the characteristic luminosity at $z \sim 5-6$ and they lie near the star-forming main sequence (e.g., Speagle et al. 2014), as shown by Faisst et al. (2016a), we refer to these galaxies as "normal" in the following. Their properties significantly differ from massive, hyperluminous starbursts and quasars, which have been studied in the most detail in ISM studies at $z > 5$ to date and are typically characterized by $\sim$5–10$\times$ higher SFRs (e.g., Riechers et al. 2014; Decarli et al. 2017). While the ultraviolet luminosity and stellar mass of all sample galaxies is approximately equal, one of the main results of our initial ALMA observations was the wide range of [C II] and dust continuum luminosity observed (Capak et al. 2015). This wide range of FIR properties already in this small sample may suggest an evolutionary sequence spanning the range from younger galaxies during their first major starburst, to more "mature" and dust-rich galaxies bridging the gap, to traditionally submillimeter-selected DSFGs (e.g., Capak et al. 2015; Pavesi et al. 2016; Faisst et al. 2017). This interpretation is supported by an analysis of the IRX/$\beta_{\rm UV}$ (IR excess - UV slope) relation (Faisst et al. 2017), which found similar conditions to those observed in massive galaxies at lower redshift in some galaxies while suggesting different dust properties (such as those observed in low-metallicity dwarfs) for others.

In order to constrain the conditions for star formation, low-J CO transitions provide the best probe and most direct comparison to lower-redshift surveys (e.g., Daddi et al. 2010a; Tacconi et al. 2013, 2018). The cold molecular gas properties in "normal" star-forming galaxies are poorly constrained beyond $z \sim 3$. Even at $z \sim 3-4$, only a few significant detections have been achieved, mostly afforded by strong gravitational lensing (Coppin et al. 2007; Riechers et al. 2010b; Dessauges-Zavadsky et al. 2015, 2017), a serendipitous detection at $z \sim 3.22$ (Gowardhan et al. 2017, 2019), and constraining upper limits for unlensed targets (e.g., Tan et al. 2013). The low detection rate could suggest a strong evolution in $\alpha_{\rm CO}$ with redshift, possibly driven by a rapid metallicity evolution (Tan et al. 2013, 2014). However, as shown by Capak et al. (2015), standard selection techniques at $z > 5$ yield a wide range of dust obscuration, which may suggest that a corresponding range of CO enrichment may also exist. We here present the NSF's Karl G. Jansky Very Large Array (VLA) observations of the CO(2–1) transition from the FIR-brightest "normal" galaxy of the Capak et al. (2015) sample and of another, approximately three times less FIR-bright, to obtain the first solid constraints at $z \sim 6$. We also discuss new ALMA measurements of the [N II] line luminosity in all of the galaxies from the Capak et al. (2015) sample with dust continuum and [C II] detections.

In Section 2, we describe new VLA observations of the CO(2–1) line transition from HZ10 ($z \sim 5.7$) and those covering LBG-1 ($z \sim 5.3$; also named HZ6; Riechers et al. 2014; Capak et al. 2015), which were initially obtained as part of the CO Luminosity Density at High-z (COLDz) survey (Pavesi et al. 2018b). We also present new ALMA observations targeting the [N II] transition at 205 μm from the dust-detected subsample among those presented by Capak et al. (2015),

composed of HZ4, LBG-1, HZ9, and HZ10, expanding our previous sample study (Pavesi et al. 2016). In Section 3 we present the results from the analysis of our CO and [N II] measurements. In Section 4 we discuss the implications of our measurements for the metallicity, the state of maturity of the star-forming ISM, and the "star formation law" of this sample of "normal" galaxies at $z > 5$. Finally, we present our conclusions in Section 5. In this work, we adopt a Chabrier IMF and a flat, ΛCDM cosmology with $H_0 = 70\,\mathrm{km\,s^{-1}\,Mpc^{-1}}$ and $\Omega_M = 0.3$.

2. Observations

2.1. VLA Observations of CO(2–1)

We observed the CO(2–1) transition in HZ10 using the VLA in the Ka band (project ID: 17A-011; PI: Pavesi). A complete description of these observations may be found in Pavesi et al. (2018a), which describes the properties of CRLE, a hyperluminous DSFG at the same redshift as HZ10 and located within the same field of view, with a separation of only 13″. In three of the eight observing sessions, the two intermediate frequencies (IFs) were tuned to the central frequency of the CO(2–1) line in HZ10 and the adjacent frequency range to maximize continuum sensitivity. In the remaining five sessions, the second IF was moved in order to provide uninterrupted coverage of the CO(2–1) line in CRLE by partially overlapping the first IF (Pavesi et al. 2018a). The total observing time was 19.8 hr on source. We imaged the data with the CLEAN algorithm in the Common Astronomy Software Application (CASA; version 4.7), using natural weighting for maximal sensitivity. The imaging of the CO line data results in a synthesized beam size of $3\farcs0 \times 2\farcs3$ at the redshifted CO(2–1) frequency and $2\farcs7 \times 2\farcs3$ in the continuum map. The rms noise at the position of HZ10 (i.e., at the phase center) is $\sim$45 μJy beam^{-1} in a 35 km s^{-1} wide channel. The final rms noise when averaging over the line-free 2.0 GHz of bandwidth is $\sim$2.7 μJy beam^{-1}. The CO(2–1) transition in LBG-1 was observed as part of the COLDz survey (Pavesi et al. 2018b; Riechers et al. 2019), and a preliminary version was shown by Riechers et al. (2014). A complete description of these observations and the imaging may be found in Pavesi et al. (2018b). The equivalent time on source in the mosaic is 14 hr at the position of LBG-1. The imaging of the CO line data results in a synthesized beam size of $2\farcs5 \times 2\farcs3$ at the redshifted CO(2–1) frequency and $2\farcs7 \times 2\farcs4$ in the continuum map. The rms noise at the position of LBG-1 is $\sim$67 μJy beam^{-1} in a 35 km s^{-1} wide channel. The final rms noise when averaging over the full 8 GHz of bandwidth is $\sim$1.3 μJy beam^{-1}.

2.2. ALMA Observations of [C II] and [N II]

Our observations of the [C II] line, data reduction, and imaging for LBG-1 and HZ10 were previously described by Riechers et al. (2014), Capak et al. (2015), and Pavesi et al. (2016). The ALMA Cycle 1 observations targeting the [C II] lines for HZ4 and HZ9 were previously presented by Capak et al. (2015), and here we provide a brief description of the data that we have reprocessed and reanalyzed. These observations were taken on 2013 November 4–16 in Band 7 as part of a larger project (ID: 2012.1.00523.S; PI: Capak). The HZ4 pointing resulted in 20 minutes on source with 28 usable antennas. Ganymede was observed as a flux calibrator, J0522 −3627 was observed as a bandpass calibrator, and J1008 +0621 was observed as an amplitude/phase gain calibrator. The HZ9 data resulted in 38 minutes on source with 27 antennas. Ganymede was observed as a flux calibrator, J1037 −2934 was observed as a bandpass calibrator, and J1058 +0133 was observed as an amplitude/phase gain calibrator. In both cases, the correlator was set up to target the expected frequency of the [C II] line and provide continuous coverage of the continuum emission in adjacent spectral windows with channels of 15.6 MHz in time division mode (TDM). CASA version 4.5 was used for data reduction and analysis. All images and mosaics were produced with the CLEAN algorithm, using natural weighting for maximal sensitivity. For HZ4, the imaging results in a synthesized beam size of $0\farcs8 \times 0\farcs5$ at the redshifted [C II] frequency and in the continuum map. The rms noise in the phase center is $\sim$0.5 mJy beam^{-1} in a 44 km s^{-1} wide channel, and the final rms noise when averaging over all spectral windows (i.e., over a total 7.5 GHz of bandwidth) is $\sim$54 μJy beam^{-1}. For HZ9, the imaging results in a synthesized beam size of $0\farcs6 \times 0\farcs5$ at the redshifted [C II] frequency and in the continuum map. The rms noise in the phase center is $\sim$0.4 mJy beam^{-1} in a 43 km s^{-1} wide channel, and the final rms noise when averaging over all spectral windows (i.e., over a total 7.5 GHz of bandwidth) is $\sim$47 μJy beam^{-1}.

Cycle 3 observations of [N II] 205 μm targeting our sample galaxies were taken on 2016 January 1 and 5 in Band 6 as part of two separate programs (2015.1.00928.S and 2015.1.00388.S; PIs: Pavesi and Lu, respectively), with one track from each program for HZ10 and LBG-1 and one track for HZ4 and HZ9 from the second program, taken in a compact configuration (max. baseline $\sim$300 m). Observations from the first program were previously described by Pavesi et al. (2016), and the HZ10 observations for both programs were previously described by Pavesi et al. (2018a). We here present the remaining observations for LBG-1, HZ4, and HZ9. The two sets of observations for LBG-1 resulted in 64 and 18 minutes on source, respectively, with $\sim$41–45 usable 12 m antennas under good weather conditions at 1.3 mm. The first set of observations was previously described by Pavesi et al. (2016). For the second set of observations of LBG-1, the nearby radio quasar J0948 +0022 was observed regularly for amplitude and phase gain calibration, and J0854+2006 was observed for bandpass and flux calibration. The observations of HZ4 and HZ9 resulted in 30 and 47 minutes on source, with 45 and 47 usable 12 m antennas, respectively. The same radio quasar was observed for amplitude and phase calibration as for LBG-1, and J1058+0133 was observed for bandpass and flux calibration. The correlator was set up in an identical configuration for these observations to cover two spectral windows of 1.875 GHz bandwidth each at 15.6 MHz ($\sim$20 km s^{-1}) resolution (dual polarization) in TDM in each sideband. We estimate the overall accuracy of the flux calibration to be within $\sim$10%. We used CASA version 4.5 for data reduction and analysis. We combined data from all observations and produced all images with the CLEAN algorithm, using natural weighting for maximal point-source sensitivity. Imaging the [N II] data for HZ4 results in a synthesized beam size of $1\farcs6 \times 1\farcs1$ at the redshifted [N II] frequency of HZ4 and in the continuum map. The rms noise in the phase center is $\sim$0.14 mJy beam^{-1} in a 44 km s^{-1} wide channel. The final rms noise when averaging over the line-free spectral windows (i.e., over a total 7.5 GHz of bandwidth) is $\sim$13 μJy beam^{-1}. Imaging the [N II] data for LBG-1 results in a synthesized beam size of $1\farcs5 \times 1\farcs2$ at the redshifted [N II] frequency of LBG-1 and in

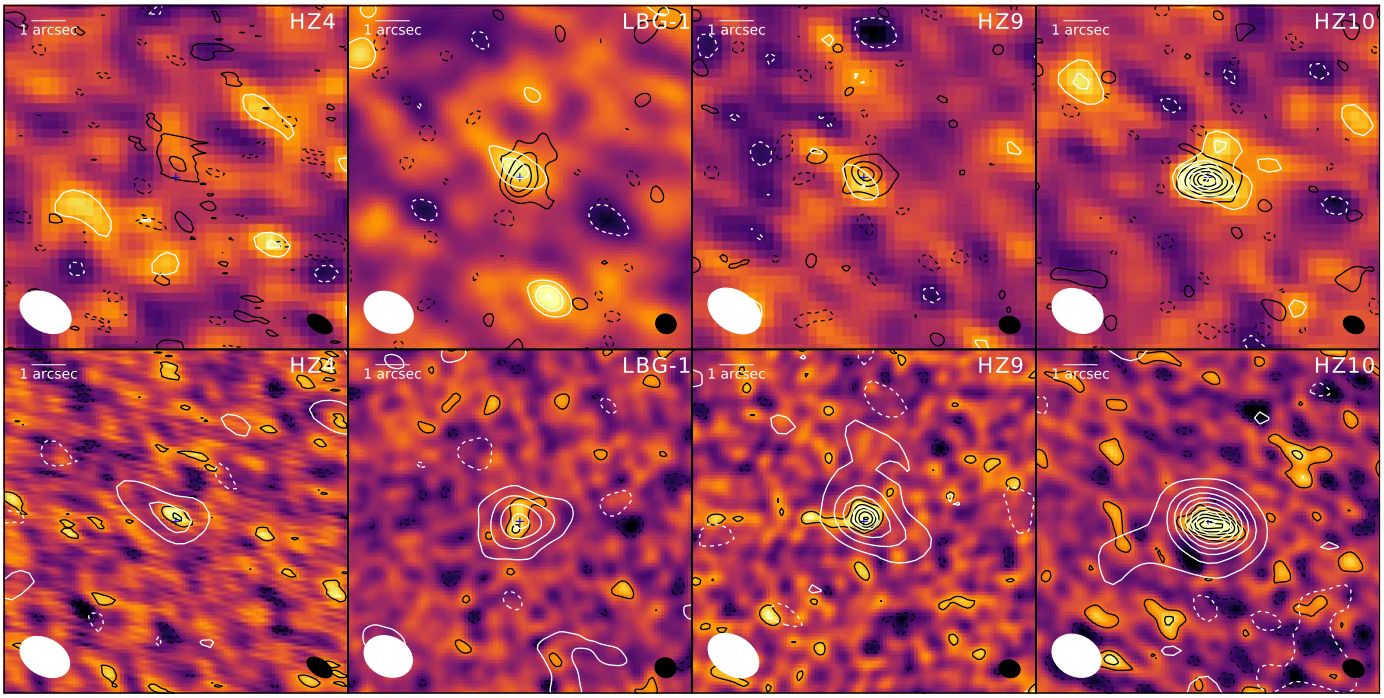

Figure 1. Top: integrated line maps (over the line FWHM) showing [N II] color scale with [N II] (white) and [C II] (black) contours overlaid. Blue plus signs indicate the positions of the 205 μm continuum peak. The [N II] ([C II]) beam is shown in the bottom left (right) corner of each panel. The [N II] ([C II]) contours are multiples of 1σ (4σ), starting at $\pm 2\sigma$. The noise levels in the [C II] line maps are 0.07, 0.04, 0.11, and 0.09 Jy km s^{-1} beam^{-1}, and in the [N II] line maps, they are 0.019, 0.016, 0.016, and 0.04 Jy km s^{-1} beam^{-1}, respectively. Bottom: continuum maps showing 158 μm color scale with 205 μm (white) and 158 μm (black) contours overlaid. Contours start at $\pm 2\sigma$ and are in steps of 2σ (with the exception of the 205 μm contours in HZ9 and HZ10, in steps of 4σ). The 205 μm (158 μm) beam is shown in the bottom left (right) corner.

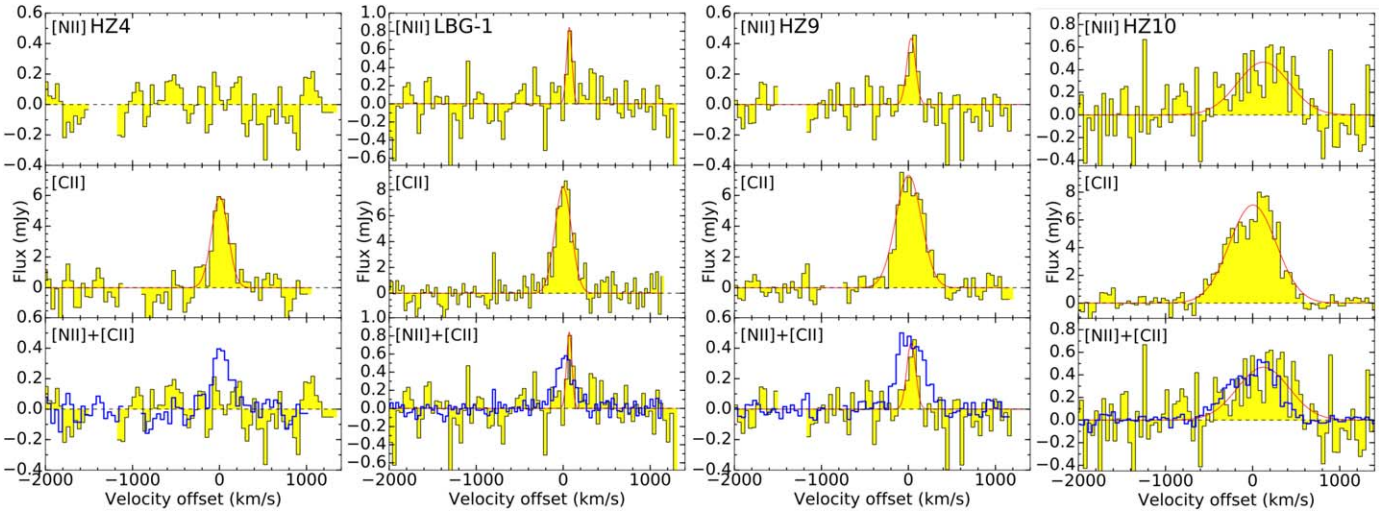

Figure 2. The [C II] and [N II] spectra of our sample galaxies and Gaussian fits to the line emission (red curves). The channel velocity width in all spectra is $\sim$42 km s^{-1} (except in the LBG-1 [C II] spectra, it is $\sim$32 km s^{-1}). Here [C II] is scaled down by a factor of 15 in flux density in the bottom panels for comparison (blue lines).

the continuum map. The rms noise in the phase center is $\sim$0.16 mJy beam^{-1} in a 40 km s^{-1} wide channel. The final rms noise when averaging over the line-free spectral windows (i.e., over a total 7.5 GHz of bandwidth) is $\sim$15 μJy beam^{-1}. Imaging the [N II] data for HZ9 results in a synthesized beam size of $1\farcs7 \times 1\farcs2$ at the redshifted [N II] frequency of HZ9 and in the continuum map. The rms noise in the phase center is $\sim$0.15 mJy beam^{-1} in a 44 km s^{-1} wide channel. The final rms noise when averaging over the line-free spectral windows (i.e., over a total 7.5 GHz of bandwidth) is $\sim$14 μJy beam^{-1}. Imaging the [N II] data for HZ10 results in a synthesized beam size of $1\farcs6 \times 1\farcs2$ at the redshifted [N II] frequency of HZ10 and in the continuum map. The rms noise in the phase center is $\sim$0.14 mJy beam^{-1} in a 44 km s^{-1} wide channel. The final rms noise when averaging over the line-free spectral windows (i.e., over a total bandwidth of 7.5 GHz) is $\sim$19 μJy beam^{-1} (Figures 1 and 2).

3. Analysis

3.1. Dust Continuum Measurements

We detect dust continuum emission from the full galaxy sample at 158 and 205 μm (Figure 1, Table 1). No continuum

Table 1
Measured CO, [C II], and [N II] Line Properties of Our Sample Galaxies

Quantity	HZ4	LBG-1	HZ9	HZ10
[C II] Line Properties				
ν_{obs} (GHz)	290.400 ± 0.013	301.980 ± 0.007	290.545 ± 0.019	285.612 ± 0.013
Redshift	5.5445 ± 0.0003	5.29359 ± 0.00015	5.5413 ± 0.0004	5.6543 ± 0.0003
$S_{[C\ II]}$ (mJy)	5.9 ± 0.7	8.2 ± 0.5	7.3 ± 0.9	7.1 ± 0.3
$FWHM_{[C\ II]}$ (km s^{-1})	230 ± 30	230 ± 20	350 ± 50	630 ± 30
$I_{[C\ II]}$ (Jy km s^{-1})	1.3 ± 0.3	2.1 ± 0.2	2.7 ± 0.3	4.5 ± 0.3
$L_{[C\ II]}$ (10^9 $L_\odot$)	1.1 ± 0.3	1.71 ± 0.16	2.2 ± 0.2	4.0 ± 0.3
Deconvolved size	(1.″1 ± 0.″3) × (0.″6 ± 0.″3)	(1.″00 ± 0.″12) × (0.″57 ± 0.″10)	(0.″68 ± 0.″12) × (0.″48 ± 0.″11)	(0.″80 ± 0.″07) × (0.″42 ± 0.″06)
Size (kpc^2)	(6.6 ± 1.8) × (3.6 ± 1.8)	(6.2 ± 0.7) × (3.5 ± 0.6)	(4.1 ± 0.7) × (2.9 ± 0.7)	(4.8 ± 0.4) × (2.5 ± 0.4)
$S_{158\ \mu m}$ (mJy)	0.24 ± 0.05	0.26 ± 0.07	0.60 ± 0.09	1.18 ± 0.16
[N II] Line Properties				
ν_{obs} (GHz)	…	232.114 ± 0.007	223.348 ± 0.009	219.49 ± 0.04
$S_{[N\ II]}$ (mJy)	…	0.8 ± 0.2	0.4 ± 0.1	4.7 ± 0.8
$FWHM_{[N\ II]}$ (km s^{-1})	…[a]	73 ± 19	120 ± 30	700 ± 130
$I_{[N\ II]}$ (Jy km s^{-1})	<0.06	0.06 ± 0.02	0.05 ± 0.02	0.34 ± 0.10
$L_{[N\ II]}$ (10^9 $L_\odot$)	<0.04	0.036 ± 0.012	0.032 ± 0.013	0.22 ± 0.07
$S_{205\ \mu m}$ (mJy)	0.10 ± 0.02	0.20 ± 0.03	0.33 ± 0.04	0.83 ± 0.05
$L_{[C\ II]}/L_{[N\ II]}$	>24	41^{+20}_{-10}	61^{+40}_{-17}	17^{+7}_{-4}
CO(2–1) Line Properties				
ν_{obs} (GHz)	…	…	…	33.157 ± 0.006
S_{CO} (mJy)	…	…	…	0.16 ± 0.03
$FWHM_{CO}$ (km s^{-1})	…	…[a]	…	650 ± 140
I_{CO} (Jy km s^{-1})	…	<0.018	…	0.10 ± 0.02
L'_{CO} (10^{10} K km s^{-1} pc^2)	…	<0.44	…	2.9 ± 0.6
$S_{34\ GHz}$ (μJy)	…	<4	…	<7.8

Notes. All quoted uncertainties correspond to 1σ statistical uncertainty intervals, and all limits correspond to 3σ.
[a] We assume an FWHM equal to that of the [C II] line in order to derive upper limits on the line flux.

Table 2
Derived Properties of Our Sample Galaxies

Quantity	HZ4	LBG-1	HZ9	HZ10
$L_{\rm FIR}$ ($10^{11}\,L_{\odot}$)	$5.2^{+4.6}_{-2.6}$	$4.9^{+4.4}_{-2.6}$	12^{+10}_{-6}	13^{+11}_{-7}
SFR ($M_{\odot}$ yr^{-1})	52^{+46}_{-26}	49^{+44}_{-26}	120^{+100}_{-60}	130^{+110}_{-70}
M_{*} ($10^{9}\,M_{\odot}$)[a]	$4.7^{+2.9}_{-1.8}$	15^{+6}_{-5}	$7.2^{+5.0}_{-2.9}$	25^{+12}_{-8}
$M_{\rm gas}$ ($10^{10}\,M_{\odot}$)[b]	...	<2	...	13 ± 3
$M_{\rm dyn}(<R_{1/2})$ ($10^{10}\,M_{\odot}$)	$1.8^{+1.3}_{-1.0}$	$1.9^{+0.6}_{-0.4}$	$3.5^{+3.1}_{-1.6}$	10 ± 3

Notes. All quoted uncertainties correspond to 1σ intervals, and all limits correspond to 3σ.
[a] Stellar masses reported by Capak et al. (2015).
[b] Gas masses are derived from the CO luminosity assuming a Galactic $\alpha_{\rm CO} \sim 4.5$ conversion factor.

signal is detected in the VLA observations targeting HZ10 and LBG-1 at ∼34 GHz (corresponding to rest frame ∼1.3 mm), yielding deep 3σ upper limits (Table 1). We measure the continuum flux at 158 and 205 μm by imaging all line-free channels using natural baseline weighting and the CASA task IMFIT to fit a 2D Gaussian model to the emission. These detections and upper limits represent the only available constraints to the FIR spectral energy distribution (SED), and we use them in the following to constrain the FIR luminosity and provide initial gas mass estimates through the Rayleigh–Jeans method.

We follow standard procedure and fit these continuum fluxes with a modified blackbody smoothly connected to a mid-IR power law (e.g., Casey 2012; Riechers et al. 2014; Pavesi et al. 2016; Faisst et al. 2017). The results of the FIR SED fitting, together with the optical-to-FIR SED for the full galaxy sample, are shown in Appendix A. We adopt a Bayesian approach and employ a Markov chain Monte Carlo (MCMC) technique through `emcee` to infer the posterior distribution for the modified blackbody parameters—dust temperature, dust emissivity β parameter, mid-IR power-law index, flux normalization, and wavelength—at which the optical depth equals unity. We adopt high dust temperature priors, as suggested by Faisst et al. (2017) for these galaxies. We employ Gaussian priors for the dust emissivity β parameter (1.7 ± 0.5), dust temperature (60 ± 15 K), mid-IR power-law index (2.0 ± 0.5), and transition rest-frame wavelength to the optically thick regime ($60 \pm 20\,\mu$m). We note that the relative fluxes at 158 and 205 μm across our sample (with ratios ranging from 1.3 ± 0.4 to 2.4 ± 0.8) suggest a diversity of dust SED shapes. We derive FIR luminosities by integrating between 42.5 and 122.5 μm (Table 2). The available constraints are not sufficient to completely resolve the degeneracy between dust temperature and emissivity index variations, which are, however, fully captured by our Bayesian approach and contribute to the uncertainties quoted for the FIR luminosity. Because the dust SEDs are not constrained in the mid-IR, we follow the standard practice of adopting the FIR luminosities as an estimate of total IR without extrapolating to shorter IR wavelengths (e.g., Riechers et al. 2014; Pavesi et al. 2018a). We caution, however, that this may be an underestimate, and that the total IR luminosity may be ∼1.5–2× higher than the FIR alone.

In order to provide constraints on the gas masses in these galaxies independently from the CO measurements, we can use the Rayleigh–Jeans dust continuum emission. This will provide the first constraints to the $\alpha_{\rm CO}$ conversion factor in "normal" galaxies at $z > 3$ in the following. The Rayleigh–Jeans dust continuum emission has been used to estimate dust and gas masses, assuming an average emissivity and dust temperature for the dominant cold dust component and a constant dust-to-gas ratio (Hildebrand 1983; Eales et al. 2012; Bourne et al. 2013; Scoville 2013; Scoville et al. 2013, 2016, 2017; Groves et al. 2015). The dependence on cold dust temperature and dust-to-gas ratio may make the Rayleigh–Jeans method less reliable than at lower redshifts (e.g., Pavesi et al. 2018a). On the other hand, the opposing effects of increasing dust temperatures and decreasing dust-to-gas ratios that may occur in "normal" galaxies at high redshift may partially compensate for each other, as also found in recent simulations that are consistent with this approach to gas mass measurement (e.g., Liang et al. 2018; Privon et al. 2018). We here adopt Equations (10) and (13) of Scoville et al. (2016) to derive gas mass estimates based on our continuum flux measurements through the same assumptions that were used in those lower-redshift samples (Scoville et al. 2016, 2017). The 34 GHz upper limits imply 3σ gas mass limits of $<2.8 \times 10^{11}\,M_{\odot}$ for HZ10 and $<1.6 \times 10^{11}\,M_{\odot}$ for LBG-1, adopting the relation derived by Scoville et al. (2016, 2017). We also use the ∼230 GHz continuum fluxes to derive approximate estimates, although these measurements may not lie on the Rayleigh–Jeans tail and therefore may not accurately trace the cold dust component. These continuum measurements would imply gas masses of $\sim 1.3 \times 10^{10}\,M_{\odot}$ for HZ4, $\sim 2.5 \times 10^{10}\,M_{\odot}$ for LBG-1, $\sim 4.4 \times 10^{10}\,M_{\odot}$ for HZ9, and $\sim 1.1 \times 10^{11}\,M_{\odot}$ for HZ10, with dominant systematic uncertainties due to the extrapolation of the method to very high redshift.

3.2. CO Measurements

We detect CO(2–1) line emission from HZ10 with a significance of $\gtrsim 8\sigma$ and provide a constraining upper limit to the CO(2–1) emission toward LBG-1 (Figure 3). We extract an aperture spectrum for HZ10[4] and a single pixel spectrum at the peak position of the [C II] emission toward LBG-1 in order to measure or constrain the CO(2–1) line properties (Table 1). The CO(2–1) emission toward HZ10 appears slightly resolved, although the coarse resolution of compact array configuration observations does not allow a precise size determination. We use CASA UVMODELFIT to fit a circular Gaussian model to the line visibilities in HZ10 and derive a deconvolved FWHM size of $1\farcs2 \pm 0\farcs4$ for the CO(2–1) emission, corresponding to 7 ± 2 kpc, which is compatible with the [C II] and [N II] size estimates. We do not make use of this size estimate in the following, but we use it to validate that the CO and [C II] emission sizes for our target are consistent within the relative uncertainties. Since we find compatible values, we will adopt [C II] emission sizes for gas reservoir sizes in the following.[5]

Our upper limit indicates that CO(2–1) line emission from LBG-1 is unexpectedly weak relative to low-redshift trends. This may be expected as a consequence of low metallicity and relatively low dust abundance (Bolatto et al. 2013) and as previously observed at $z > 1$ on multiple occasions (e.g., Genzel et al. 2012; Tan et al. 2014). Here LBG-1 shows an unusually high inferred [C II]/CO(1–0) luminosity ratio ($\gtrsim$9000; Figure 3) relative to the value in HZ10 (∼3000), the

[4] We adopt elliptical apertures of sizes equal to the FWHM of the best-fit 2D Gaussian to the integrated line emission.
[5] This is a common assumption, since both CO and [C II] trace the extent of the gas distribution (e.g., De Breuck et al. 2014; Litke et al. 2019).

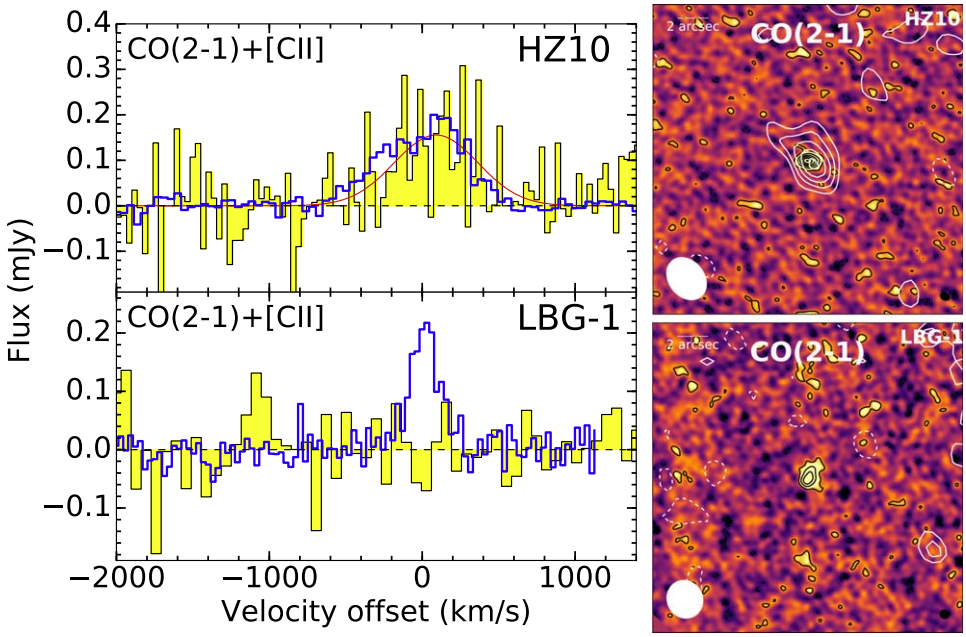

Figure 3. Left: CO(2–1) spectra of HZ10 and LBG-1 and Gaussian fit to the detected line emission (red curves). Here [C II] is shown scaled down by a factor of 40 in flux density for comparison (blue lines). The channel velocity width is ∼40 km s^{-1} for HZ10 in both spectra and ∼32 and ∼64 km s^{-1} for LBG-1 for [C II] and CO, respectively. Right: integrated line maps (over the line FWHM) showing [C II] color scale with CO(2–1) (white) and [C II] (black) contours. The CO(2–1) ([C II]) beam is shown in the bottom left (right) corner of each panel. The CO(2–1) ([C II]) contours are multiples of 1σ (4σ), starting at ±2σ. The noise levels in the [C II] line maps are 0.04 and 0.09 Jy km s^{-1} beam^{-1} for LBG-1 and HZ10, respectively, and in the CO(2–1) line maps are 0.006 and 0.010 Jy km s^{-1} beam^{-1} for LBG-1 and HZ10, respectively.

values commonly measured in local starbursts and high-redshift galaxies (∼4400; e.g., Wolfire et al. 1989; Stacey et al. 1991, 2010), and a sample of high-redshift DSFGs (5200 ± 1800; e.g., Gullberg et al. 2015). The high ratios observed in LBG-1 cannot be explained within standard photodissociation region (PDR) models, but they naturally arise as a consequence of lower metallicity (e.g., Maloney & Black 1988; Stacey et al. 1991; Madden et al. 1997). In particular, low-metallicity dwarf galaxies typically show similar ratios of ∼7000–10^5 (e.g., Cormier et al. 2014; Jameson et al. 2018). On the other hand, the normal ratio observed in HZ10 points to star-forming gas properties that are similar to what is observed in lower-redshift main-sequence galaxies.

The CO(2–1) line luminosity is expected to provide a reliable estimate of the molecular gas mass. However, several factors affect the proportionality factor, such as heating from and contrast against the cosmic microwave background (CMB; e.g., da Cunha et al. 2013) and the strong metallicity dependence of the CO luminosity per unit molecular gas mass (e.g., Bolatto et al. 2013). Current samples including both DSFGs and main-sequence galaxies at high redshift show nearly thermalized gas excitation up to the $J = 2$–1 transition ($R_{21} \sim 0.80$–0.95; e.g., Carilli & Walter 2013; Daddi et al. 2015). Here, we therefore assume a brightness temperature ratio of $R_{21} = 1$ between the CO $J = 2$–1 and 1–0 transitions. The CMB contributions at $z > 5$ are only weakly constrained without additional CO excitation measurements. Da Cunha et al. (2013) suggested that we may expect the observed CO line flux to be suppressed by a factor of ∼1.25–2 at this redshift. We do not attempt to estimate this effect independently but simply absorb it into the definition of $\alpha_{\rm CO}$.

We can use the gas mass estimates based on the Rayleigh–Jeans dust continuum emission to constrain the $\alpha_{\rm CO}$ conversion factor by assuming that the gas mass is dominated by molecular gas. The main uncertainties inherent in the Rayleigh–Jeans dust method are a dependence on the gas-to-dust ratio and dust properties affecting the dust SED. The effects of these uncertainties dominate over the CO and dust continuum measurement uncertainties. The gas mass estimates presented in Section 3.1 imply constraints to $\alpha_{\rm CO}$ of[6] $\lesssim$10 (∼4 based on the 220 GHz flux) for HZ10 and $\gtrsim$5.7 based[7] on the 230 GHz flux for LBG-1. These estimates are dominated by the systematic uncertainty inherent in extrapolating the Rayleigh–Jeans method to very high redshift, where it has not yet been validated. These approximate estimates are in agreement with our inference of "normal" star-forming gas properties for HZ10, with $\alpha_{\rm CO}$ near the Milky Way value, and of lower-metallicity gas in LBG-1, as signaled by an elevated $\alpha_{\rm CO}$.

3.3. Dynamical Mass and Gas Mass Constraints

In order to estimate dynamical masses for the full galaxy sample, we adopt a commonly used empirical procedure based on the line width and gas emission size inferred from the integrated line emission that was calibrated on disk galaxy simulations (e.g., Daddi et al. 2010a). The advantage of such a method is the applicability to our full galaxy sample and a more straightforward comparison to most dynamical mass estimates available in the literature, which typically rely on such estimates

[6] Units of $M_\odot$(K km s^{-1} pc^2)$^{-1}$ assumed throughout the following.

[7] In order to deal with relative uncertainties of order unity throughout this work, we adopt the convention of quoting Gaussian-equivalent percentiles. Therefore, uncertainty ranges correspond to 16th, 50th, and 84th percentiles, and 3σ limits are defined to imply a 99.7% probability. Propagation of these uncertainties to derived quantities was carried out by numerical sampling and evaluation of posterior distribution percentiles. Lognormal distributions were used to sample skewed distributions described by asymmetric 1σ ranges. Upper limits from nondetections are treated as positive-truncated (enforcing a uniform prior), zero-centered Gaussians with a specified standard deviation as determined by the noise level.

(e.g., Tacconi et al. 2008; Förster Schreiber et al. 2009; Engel et al. 2010; Walter et al. 2012; Carilli & Walter 2013; Riechers et al. 2014; Capak et al. 2015; Decarli et al. 2016; Oteo et al. 2016; Venemans et al. 2016). We apply this technique by using the line FWHM, the fitted half-light radii of the [C II] emission, and the disk inclination from the ratio of minor to major axes (Table 2). The inferred dynamical mass for LBG-1 is ∼2.5 times lower than previous estimates, although within the original uncertainties, due to a revised [C II] size and differences in the method employed (Riechers et al. 2014). However, dynamical mass estimates for LBG-1 may be affected by complex velocity structure due to interactions.

In Appendix B we present an alternative dynamical analysis that directly models the observed visibilities,[8] following the method previously described by Pavesi et al. (2018a). The inferred dynamical mass estimates are in agreement with those derived by Jones et al. (2017) based on tilted-rings modeling in the image plane and with those based on the Daddi et al. (2010a) method for HZ9 and HZ10.

We can therefore use our dynamical masses to provide approximate estimates of the total gas masses in the full sample by accounting for the contribution of stellar[9] and dark matter masses (25%) following Daddi et al. (2010a). Using the CO line luminosity measurements and limits in HZ10 and LBG-1, these independent gas mass estimates allow us to place the first constraints on the $\alpha_{\rm CO}$ conversion factor in normal galaxies at this redshift. The dynamical mass estimates would imply total gas masses of $(1.4 \pm 0.9) \times 10^{10}\,M_\odot$ for LBG-1, $4.5^{+4.5}_{-2.5} \times 10^{10}\,M_\odot$ for HZ9, and $(1.2 \pm 0.5) \times 10^{11}\,M_\odot$ for HZ10. If we assume this gas mass to be dominated by molecular gas and thus divide by the CO line luminosity constraints,[10] these estimates imply an $\alpha_{\rm CO}$ (in units of $M_\odot$(K km s^{-1} pc^2)$^{-1}$) of $4.2^{+2}_{-1.7}$ for HZ10 but do not provide a significant constraint for LBG-1.[11] The estimated $\alpha_{\rm CO}$ factor for HZ10 is compatible with the Milky Way value (∼4.5 in the same units; Bolatto et al. 2013), which may also apply to $z \sim 1-2$ main-sequence disk galaxies (Daddi et al. 2010a; Carilli & Walter 2013; Tacconi et al. 2013; Genzel et al. 2015). In the following, we assume a fixed value of $\alpha_{\rm CO} = 4.5$ for definiteness in order to derive and constrain gas masses in HZ10 and LBG-1 (Table 2, Figure 4), with the caveat that this value may only be a lower limit in the case of LBG-1 due to metallicity effects (e.g., Bolatto et al. 2013).

3.4. Constraints on High-redshift Star Formation

To study the star formation efficiency in HZ10 and LBG-1, we first directly compare the FIR to the CO luminosity, in relation to the expectations based on previous determinations of the star formation law in the local and high-redshift universe (Carilli & Walter 2013). Daddi et al. (2010b) and Genzel et al. (2010) measured a relationship between the CO luminosity and the SFR (or IR luminosity) for lower-redshift main-sequence disk galaxies, which is indicative of an underlying "star formation law" and found broad agreement within the significant scatter of the observed correlation. Here we aim to investigate its evolution toward higher redshift. The relationship by Daddi et al. (2010b) would predict total IR luminosities of $(2.3 \pm 0.5) \times 10^{12}\,L_\odot$ for HZ10 and $<2.7 \times 10^{11}\,L_\odot$ for LBG-1, respectively, based on the CO luminosity, which is compatible with our direct FIR luminosity estimates. Therefore, we find no evidence for an evolution in the star formation law for main-sequence galaxies all the way up to $z \sim 6$, although larger samples are necessary to statistically assess this finding.

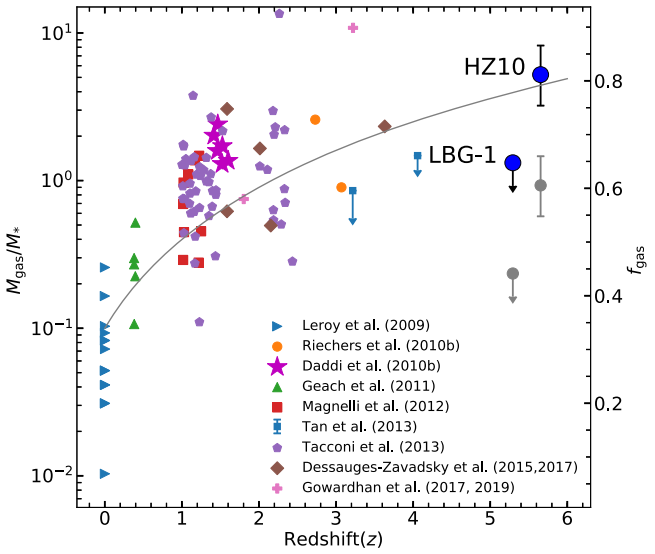

Figure 4. Ratio of molecular gas mass to stellar mass (calculated using $\alpha_{\rm CO} = 4.5\,M_\odot$(K km s^{-1} pc^2)$^{-1}$ for all sources) adapted from Carilli & Walter (2013), Daddi et al. (2010a), Dessauges-Zavadsky et al. (2015, 2017), Geach et al. (2011), Gowardhan et al. (2017, 2019), Leroy et al. (2009), Magnelli et al. (2012), Riechers et al. (2010b), Tacconi et al. (2013) and Tan et al. (2013) The gray line shows $M_{\rm gas}/M_* \propto (1+z)^2$ (Geach et al. 2011). An alternative choice of $\alpha_{\rm CO} = 0.8$ for HZ10 and LBG-1 is also shown in light gray. Stellar masses are adopted from Capak et al. (2015).

Adopting our best estimate of the gas mass and SFR in HZ10 (Table 2) yields a gas depletion timescale (the inverse of the star formation efficiency) of 960^{+1200}_{-470} Myr,[12] which is significantly longer than what is commonly measured in local and high-redshift starburst galaxies ($\lesssim$100 Myr; e.g., Carilli & Walter 2013). Therefore, HZ10 appears to be very rich in molecular gas, and the efficiency of star formation appears compatible with what is commonly observed in lower-redshift, disklike, main-sequence galaxies (0.5–2 Gyr; e.g., Leroy et al. 2013; Tacconi et al. 2013, 2018).

The IR luminosity of LBG-1 is at least a factor of 2 higher than estimates based on its CO luminosity and the star formation law, suggesting that the CO luminosity in LBG-1 is lower than that in lower-redshift galaxies with comparable SFR (Figure 5). If we adopt our best estimates for the SFR in LBG-1 based on the inferred IR luminosity, we can obtain estimates of the gas depletion timescale for the gas masses derived from the

[8] The main advantage of such visibility-based rather than image-based approaches is independence from deconvolution and imaging and the statistical dependence of image pixels introduced by the nonlocal synthesized beam.

[9] Stellar masses for all of our galaxies are constrained by the rich multiwavelength coverage available in the COSMOS field, were measured by Capak et al. (2015) and Laigle et al. (2016) for the entire parent sample, and are typically uncertain to within a factor of ∼2 (Table 2). The stellar mass fits include deep (25.5 AB mag) COSMOS/SPLASH (Steinhardt et al. 2014) *Spitzer*/IRAC photometry to probe wavelengths redder than rest frame 4000 Å, which is crucial for constraining stellar masses to this accuracy (e.g., Faisst et al. 2016b; Laigle et al. 2016). However, we caution that stellar masses at $z > 4$–5 are difficult to constrain because the rest-frame 1–2 μm wavelength emission, which is the most accurate tracer, will not be observable in such faint galaxies at $z > 5$ until the *James Webb Space Telescope* becomes operational.

[10] Following the procedure explained in footnote 7.

[11] Due to the large uncertainty in the gas mass estimate, the 3σ CO limit only implies a 3σ limit of $\alpha_{\rm CO} > 0.2$ when appropriately propagated through posterior sampling. See footnote 7.

[12] Uncertainties were propagated from both the SFR and the gas mass estimates.

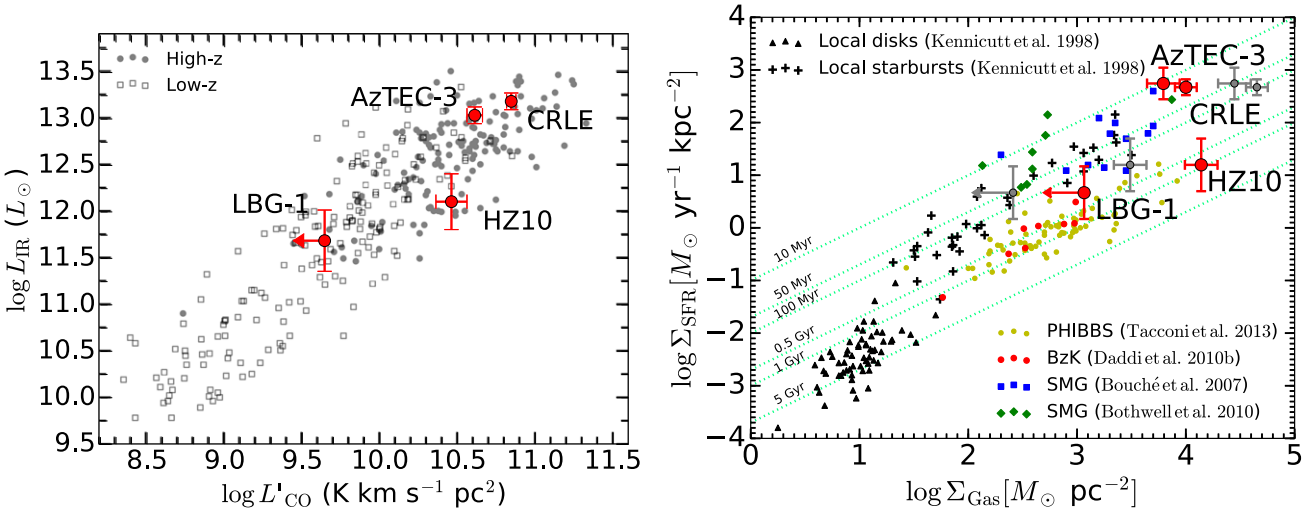

Figure 5. Left: IR luminosity observed in a sample of local and high-redshift galaxies as a function of their CO luminosity for comparison to the measurements in HZ10 and LBG-1 (Carilli & Walter 2013). We also include two $z > 5$ DSFGs for reference (AzTEC-3 and CRLE; Riechers et al. 2010a, 2014; Pavesi et al. 2018a, 2018b), clearly occupying a distinct part of the parameter space. Right: SFR surface density as a function of the gas mass surface density for a sample of local and high-redshift galaxies, including HZ10, LBG-1, AzTEC-3, and CRLE (adapted from Daddi et al. 2010b, updated by Tacconi et al. 2013). The SFR surface density was estimated for the $z > 5$ galaxies through the FIR luminosity and dust continuum sizes. The gas surface density was estimated uniformly for these galaxies through the CO luminosity and the [C II] emission spatial size, which is compatible with our current constraints on the CO emission size. Following Daddi et al. (2010b), we adopt $\alpha_{\rm CO} \sim 4.5$ for main-sequence galaxies such as HZ10 and LBG-1 and the other disk galaxies and $\alpha_{\rm CO} = 0.8$ for starbursts such as CRLE, AzTEC-3, local starbursts, and high-z SMGs. Fixed gas depletion time (corresponding to fixed star formation efficiency) lines are shown for characteristic timescales spanning 10 Myr to 5 Gyr (green lines).

long-wavelength dust method ($\sim 500^{+500}_{-250}$ Myr), dynamical mass constraints ($\sim 280^{+420}_{-180}$ Myr), and CO upper limit ($\lesssim$2.8 Gyr) with 99.7% probability when assuming $\alpha_{\rm CO} = 4.5$.

We can also use our estimates for the gas reservoir physical sizes derived from the [C II] line to compare the gas surface density to the SFR density probed by the dust continuum flux and size (Figure 5), probing the physical drivers of star formation more directly, i.e., the Kennicutt–Schmidt law (Kennicutt 1998; Bigiel et al. 2008, 2011; Leroy et al. 2008; Daddi et al. 2010b; Schruba et al. 2011; Kennicutt & Evans 2012; Leroy et al. 2013). Specifically, we include in this comparison both main-sequence galaxies at $z \sim$ 1–3 (Tacconi et al. 2013; Daddi et al. 2010b) and intensely star-forming submillimeter galaxies (SMGs; Bouché et al. 2007; Bothwell et al. 2010). In particular, we focus our comparison on CRLE and AzTEC-3, two hyperluminous DSFGs at $z > 5$ that are located in physical proximity to HZ10 and LBG-1, respectively. Based on their global gas masses and SFR, the gas depletion timescales for CRLE and AzTEC-3 are ~45–50 Myr (Riechers et al. 2010a, 2014; Pavesi et al. 2018a), i.e., an order of magnitude shorter than we observe in HZ10 and LBG-1. We divide each of the SFRs and gas masses by the area within the FWHM of the best-fit elliptical Gaussian source model (e.g., De Breuck et al. 2014; Spilker et al. 2016; Litke et al. 2019) uniformly for our sample of two "normal" and two starburst galaxies at $z =$ 5–6. Following Riechers et al. (2014), Spilker et al. (2016), and Hodge et al. (2016), we use the dust continuum sizes at 158 μm as representative of the extent of the star-forming region, since the emission at such short wavelength is dominated by the actively star-forming region. We follow De Breuck et al. (2014) and Litke et al. (2019) in using the [C II] line emission size as a proxy for the extent of the gas reservoir.[13] Due to the compactness of the star formation in AzTEC-3 and CRLE, the local depletion timescales characterizing the ratio of gas and SFR surface densities are as short as ~10–30 Myr, while our estimates for HZ10 and LBG-1 are ~1 Gyr and $\lesssim$300 Myr, respectively (Figure 5). Therefore, the physical efficiency in terms of surface densities may potentially differ by up to 2 orders of magnitude already among these galaxies at $z > 5$. The comparison shown by Figure 5 shows that, while AzTEC-3 and CRLE have high star formation efficiency compatible with other high-redshift starbursts, HZ10 (and, to a lesser degree, LBG-1) appear to exhibit the lower efficiencies and longer depletion times typically observed in main-sequence disks at lower redshift. Although the depletion time measurement in HZ10 is incompatible with that in starbursts (e.g., Silverman et al. 2015, 2018), the systematic uncertainty implies compatibility with both the efficiency in $z \sim 0$ disk galaxies (e.g., Leroy et al. 2013) and the potentially higher efficiency suggested for main-sequence galaxies by Tacconi et al. (2013, 2018), Genzel et al. (2015), and Scoville et al. (2016, 2017).

3.5. [N II] Measurements

To complement our view of the star-forming gas in our sample galaxies, we observed the [N II] 205 μm line emission, which is one of the best tracers of the ionized component of the ISM. The [C II]/[N II] line ratio is the tool of choice to determine the fraction of [C II] emission coming from ionized gas (e.g., Oberst et al. 2006; Decarli et al. 2014; Pavesi et al. 2016). This quantity is itself a probe of the physical conditions of the gas, which is directly exposed to recent star formation, and may be a probe of the radiation intensity and hardness and hence, indirectly, the gas-phase metallicity. Metallicity directly affects our interpretation of CO observations (since it is one of the main drivers of the variation in $\alpha_{\rm CO}$), and it offers unique insights into the balance between fresh gas inflow and ISM enrichment through previous star formation. The analysis in

[13] Spilker et al. (2016) and Calistro Rivera et al. (2018), among others, clarified the importance of not inferring the gas reservoir extent from dust continuum sizes in this context.

this section expands on the previous analysis presented by Pavesi et al. (2016).

We tentatively detect [N II] 205 μm emission toward LBG-1 (at $\sim$3.4σ) and HZ9 (at $\sim$3.1σ), confidently detect it from HZ10 (at $\gtrsim$6σ), and provide a constraining upper limit for HZ4 (Figures 1 and 2). We confirm previous results on LBG-1 and HZ10 (Pavesi et al. 2016) by achieving a higher signal-to-noise ratio. We measure [N II] and [C II] line properties using aperture spectra consistently for the whole sample (Table 1; see footnote 4). The [N II] emission from HZ10 appears extended at limited significance ($\sim$2σ–3σ; Figure 1). In order to measure the [N II] emission size, we fit a circular Gaussian model to the integrated [N II] line visibilities from HZ10 using CASA UVMODELFIT. We estimate a deconvolved [N II] spatial FWHM size of $1\farcs71 \pm 0\farcs25$ for HZ10, formally corresponding to 10 ± 2 kpc. We use the same technique to measure an effective circular [C II] size of $0\farcs61 \pm 0\farcs04$, corresponding to 3.6 ± 0.2 kpc, which is compatible with our more sophisticated *uv*-plane modeling (Appendix B). The [N II] line emission could be marginally more extended than the [C II] emission, but higher-resolution and higher signal-to-noise [N II] observations are necessary to confirm this tentative finding. In particular, a manual inspection of the UV radial profile of the [N II] line visibilities appears compatible with the size of the [C II] emission within the relative uncertainties.

We do not detect spatial offsets between the [N II] and [C II] line emission in LBG-1, HZ9, and HZ10. Although we now confirm that the [N II] line emission in HZ10 comes from the full [C II] velocity range, the comparison of the [N II] and [C II] spectra (Figure 2) suggests a possible differential intensity ratio, with stronger [N II] intensity coming from the red part of the emission that dominated the lower signal-to-noise detection found by Pavesi et al. (2016). The [N II] line velocity width appears narrower than [C II] toward LBG-1 and HZ9 at the current sensitivity of our measurements, although the limited signal-to-noise does not allow for a reliable measurement of the line widths.

To enable a more comprehensive study, here we update our measurement of the [C II]/[N II] line ratio for HZ10 and LBG-1 (Pavesi et al. 2016), and we expand the sample to include HZ9 and HZ4 (Table 1, Figure 6). We confirm the relatively low line ratio for HZ10, which is compatible with most local and high-redshift active star-forming galaxies (Pavesi et al. 2016). On the other hand, we find substantially higher ratios for HZ9, LBG-1, and HZ4, which are only compatible with the ratio observed in local dwarf galaxies (Figure 6) and provide further evidence for the diversity of conditions at $z > 5$ already present in this small sample.

As previously described by Pavesi et al. (2016), a high [C II]/[N II] line ratio may be expected in the case of very high gas density or high intensity and hardness of the radiation field. The latter explanation appears consistent with observations of a high line ratio in local dwarf galaxies by Cormier et al. (2015), which may be interpreted as the consequence of high radiation intensity and hardness due to low-metallicity conditions. A high intensity and hardness radiation field are expected to induce higher ionization states in the ionized gas. This implies weak [N II] and [C II] emission from ionized gas because nitrogen, carbon, and oxygen are expected to be in a higher ionization state. This prediction is testable by observing strong [N III] 57 μm and [O III] 52 or 88 μm emission lines.

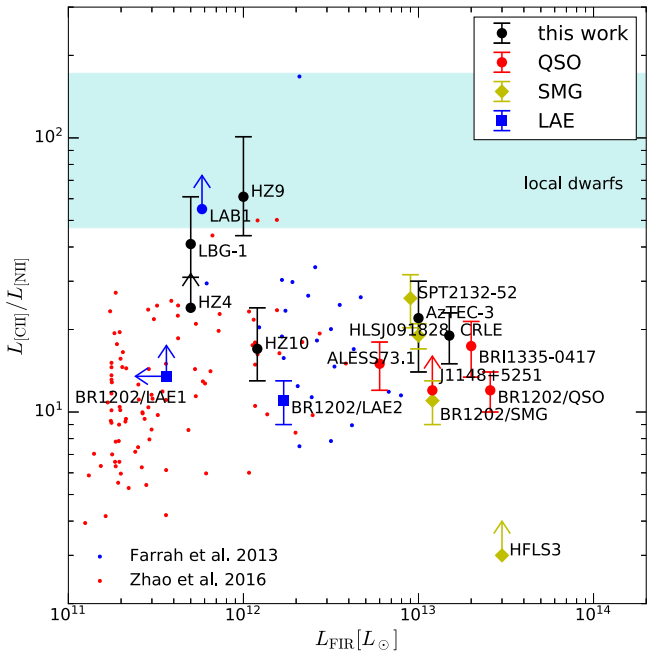

Figure 6. The [C II]/[N II] line luminosity ratios observed in high-redshift galaxies to date as a function of their FIR luminosity (Wagg et al. 2010; Combes et al. 2012; Carilli & Walter 2013; Carilli et al. 2013; Riechers et al. 2013, 2014; De Breuck et al. 2014; Rawle et al. 2014; Capak et al. 2015; Béthermin et al. 2016; Umehata et al. 2017; Lu et al. 2018; Pavesi et al. 2018a). For comparison, we also show a sample of local ULIRGs from Farrah et al. (2013; using the [N II] 122 μm line) and LIRGs with [N II] (using the [N II] 205 μm line) from Zhao et al. (2016) and [C II] from Díaz-Santos et al. (2013). The range of ratios in dwarfs (Cormier et al. 2015; using the [N II] 122 μm line) is shown as a cyan band. The [N II] 122 μm line measured in the indicated local samples was converted to an [N II] 205 μm luminosity assuming a ratio of 1/2.5, estimated by Herrera-Camus et al. (2016). The abscissa in the local samples are defined as total IR luminosity; no attempt was made to convert to a common FIR luminosity scale because it does not affect our interpretation.

Croxall et al. (2017) recently confirmed this interpretation using observations of local star-forming galaxies from the KINGFISH sample. They conclusively reported a strong correlation of the [C II]/[N II] line ratio with gas-phase metallicity, concluding that metallicity appears to be the main driver of this line ratio. Therefore, in analogy to the case of local dwarf galaxies, we interpret our high line ratio measurements and limits for HZ9, LBG-1, and HZ4 as indicative of low gas (and stellar) metallicity relative to $z < 5$ galaxies of comparable masses ($\sim 10^{10}\,M_\odot$). On the other hand, the lower line ratio observed in HZ10 suggests higher metallicity in this galaxy, confirming the inference based on high dust and CO emission and suggesting a particularly "mature, normal" galaxy at the same epoch (see also discussion by Faisst et al. 2017). We note that an alternative interpretation for the low [N II] luminosity in our high-redshift sample may invoke lower nitrogen abundance relative to carbon. While this abundance ratio change may also be a consequence of low-metallicity conditions due to the secondary nature of nitrogen, the carbon abundance dependence on gas-phase metallicity is not well constrained. We follow Díaz-Santos et al. (2017) and assume a line ratio of 3 ± 0.5 in the ionized gas to infer fractions of [C II] coming from PDRs of 83% $\pm$ 6% for HZ10, 96% $\pm$ 2% for HZ9, 93% $\pm$ 3% for LBG-1, and >86% for HZ4.

4. Discussion

The detection of bright CO emission from HZ10 represents the highest-redshift CO detection from a "normal," main-sequence galaxy to date (the next-highest-redshift CO line from an unlensed main-sequence galaxy was serendipitously detected by Gowardhan et al. 2017, 2019 at $z \sim 3.2$). We note that HZ10 appears to have a very high gas fraction based on the measured CO luminosity ($M_{\rm gas} > M_{\rm stars}$ with high confidence and likely $M_{\rm gas} \sim 4-5 \times M_{\rm stars}$; Figure 4). Such high gas fractions may be expected at $z > 5$ based on the extrapolation of observed trends (e.g., Magdis et al. 2012; Genzel et al. 2015; Tacconi et al. 2018). A high gas fraction may also potentially be connected with the possibility of a galaxy merger in HZ10, since merging galaxies have been found to potentially show enhanced gas fractions (e.g., Pavesi et al. 2018b). Assuming $\alpha_{\rm CO} \sim 4.5$ would imply a $\gtrsim$4 times lower gas fraction for LBG-1, potentially suggesting significant scatter within the general population. However, the low CO luminosity in LBG-1 is likely to be due to low metallicity, as suggested by the faint [N II] emission, and the gas fraction may therefore be substantially higher in practice.

Zavala et al. (2018) recently reported observations of CO and [C II] emission lines from the strongly lensed galaxy G09 83808 at $z \sim 6$, presenting analogies with HZ10. Although the inferred CO(1–0) luminosity of G09 83808 is approximately three times lower than that of HZ10, the dust continuum emission is at least twice as bright at rest frame 158 μm, indicating a significantly higher star formation efficiency than found in HZ10. Therefore, while G09 83808 appears to have only few times higher SFR than HZ10, its star formation properties resemble starbursts such as CRLE and AzTEC-3, while HZ10 is more gas-rich and exhibits star-forming conditions compatible with lower-redshift main-sequence disk galaxies. This finding is in agreement with the 10 times higher [C II]/FIR ratio in HZ10 relative to G09 83808. This ratio is a probe of the local physical density of star formation and is inversely proportional to the starburst intensity. Based on PDR models, a fixed PDR gas density implies that the far-UV (FUV) field intensity (G_0) scales inversely with [C II]/FIR (to a power of ~1–1.2; Wolfire et al. 1990; Kaufman et al. 1999; Stacey et al. 2010). This scaling implies that the FUV intensity in G09 83808 may be ~10–15 times higher than in HZ10, confirming that HZ10 may be forming stars in a much less intense environment.

The finding of significant dust and, especially, CO emission from HZ10 suggests that a fraction of "normal" galaxies (not extreme starbursts) at $z > 5$ may be rich in molecular gas and significantly metal-enriched, in contrast to some previous indications (e.g., Tan et al. 2013, 2014). This finding is in agreement with the recent measurement of a high volume density of CO-selected galaxies at $z > 5$ by the COLDz project (Pavesi et al. 2018b; Riechers et al. 2019). Although the galaxies selected by COLDz at $z > 5$ are bright starbursts, their volume density is significantly higher than that predicted by current models (Riechers et al. 2019). If HZ10 had been located within the COLDz field of view, it would have been selected by the blind line search based on the survey detection limit (Pavesi et al. 2018b), therefore placing an upper limit on the volume density of evolved, gas-rich "normal" galaxies at $z > 5$ with CO luminosity greater than HZ10 of $\lesssim 5 \times 10^{-5}$ Mpc^{-3} (Riechers et al. 2019).

HZ10 is believed to reside in a galaxy overdensity at $z \sim 5.7$, potentially indicating a protocluster environment (Pavesi et al. 2018a). In particular, the presence of the bright hyperstarburst CRLE only ~70 kpc away constitutes evidence of a possible physical association. This association with the massive, dusty galaxy CRLE and the protocluster may be related to the advanced evolutionary stage of HZ10. If this connection were confirmed, it would point to a more rapid evolution for galaxies in higher-density environments (e.g., Chiang et al. 2017).

The PHIBBS survey has measured star formation efficiency and gas fractions for lower-redshift main-sequence galaxies (up to $z \sim 2-3$; Tacconi et al. 2013; Genzel et al. 2015; Tacconi et al. 2018). Based on the extrapolation of the latest measured trends reported by Tacconi et al. (2018) combining the PHIBBS CO measurements with the dust-based estimates by Scoville et al. (2016, 2017), we can estimate the average gas fractions and depletion times expected for main-sequence galaxies such as HZ10 at $z \sim 5.7$. We derive an approximate gas depletion timescale of ~400 Myr, which is compatible with our estimate for HZ10 within 1σ. The molecular gas fraction predicted by the fitting formula suggested by Tacconi et al. (2018) is $M_{\rm gas} \sim M_{\rm stars}$,[14] which is lower than that observed in HZ10. Our observations therefore suggest that the increase in molecular gas fraction with redshift may continue beyond $z \sim 3$, although with limited statistical power due to the small sample size. In summary, HZ10 shows the characteristic properties of lower-redshift main-sequence galaxies all the way back to the first billion yr of cosmic time.

Vallini et al. (2018) presented some of the latest models of the CO line emission from "normal" galaxies at $z > 5$. They modeled the radiative transfer affecting CO emission from a clumpy molecular medium in an $M_{\rm stars} \sim 10^{10} M_{\odot}$ main-sequence galaxy at $z \sim 6$. Although their model galaxy is characterized by subsolar (0.5 $Z_{\odot}$) metallicity, they predicted a low effective CO conversion factor of $\alpha_{\rm CO} \sim 1.5$ due to the dominant effect of warmer gas, high turbulence, and high gas surface density (Vallini et al. 2018). While such a low $\alpha_{\rm CO}$ may be allowed for HZ10, it is ruled out for the more typical LBG-1 if the gas mass is predominantly molecular. In addition, the predicted CO luminosity for the "typical" model galaxy is ~20 times lower than that observed in HZ10, suggesting that the molecular gas mass may be significantly underestimated. Therefore, HZ10 may be more mature and therefore analogous not to the model galaxy but rather to the lower-redshift main-sequence galaxies observed at $z \sim 2-3$. Although our constraints for the CO luminosity in LBG-1 are compatible with the model predictions, the higher dynamical mass estimates suggest higher gas masses for LBG-1 than the molecular mass predicted by the models. A possible interpretation of this result may invoke a significant fraction of gas in the atomic phase, which may dominate the total gas mass in such "typical" massive galaxies. Based on the [C II] luminosity in LBG-1, we can derive an estimate of the atomic PDR mass of ~2–5 $\times 10^9 M_{\odot}$ (following Stacey et al. 1991), which may be comparable to the molecular gas mass for low $\alpha_{\rm CO}$, but it is unlikely to provide the total gas mass inferred from our dynamical mass estimate.

The measurement of [C II] and dust continuum emission from the first sample of "normal," rest-UV-selected galaxies

[14] The quadratic fitting formula predicts, perhaps artificially, a turnover of the trend at $z \sim 3.5$.

revealed a variety of star-forming conditions (Capak et al. 2015). The finding of bright CO line emission from HZ10 and faint emission from LBG-1 is in agreement with the interpretation of a range of metallicities and dust-to-gas ratios being the main contributors to the variation within the sample (Capak et al. 2015). This interpretation is strongly supported by the significant difference in [C II]/[N II] ratios between HZ10 and LBG-1 already noted by Pavesi et al. (2016). Faint [N II] emission relative to [C II] directly implies (with the possible caveat of differences in the C/N abundance ratio) a low contribution of the ionized gas to the [C II] emission, which may therefore be predominantly due to emission from neutral PDRs. The simplest interpretation for faint [N II] emission suggests higher ionization conditions in the ionized gas, predicting bright [N III] and [O III] emission instead. This interpretation would suggest that intensity and especially hardness of the radiation field may be the most relevant physical parameter affecting this line ratio. Recent detections of bright [O III] 88 μm line emission at high redshift support this interpretation and suggest that [O III] may be even brighter than [C II] in "normal" galaxies at very high redshift (e.g., Inoue et al. 2016; Carniani et al. 2017; Laporte et al. 2017; Hashimoto et al. 2018a, 2018b, 2019; Marrone et al. 2018; Tamura et al. 2019), as typically observed in local dwarfs (Cormier et al. 2015). Furthermore, recent optical studies of LBGs and LAEs have also found increasing [O III] λ5008 brightness at high redshift, together with high sSFR and low metallicity (e.g., Strom et al. 2017, 2018). The metallicity dependence may also be responsible for the downturn due to reduced oxygen abundance at even lower metallicity (Harikane et al. 2018).

Faisst et al. (2017) explored the level of maturity, stellar population properties, and dust attenuation in $z = 5$–6 "normal" galaxies through the IRX/$\beta_{\rm UV}$ diagnostic plane. While IRX, defined as the ratio $L_{\rm IR}/L_{\rm UV}$, represents the prevalence of dust-obscured star formation, $\beta_{\rm UV}$ is the power-law slope of the UV emission, which bears the imprint of dust reddening. A correlation between these quantities was observed to hold for local starburst galaxies and approximately hold up to high redshift (e.g., Meurer et al. 1999; Reddy et al. 2006, 2010, 2018; Bouwens et al. 2016); however, variations may be expected due to varying dust properties, star formation geometry, and stellar population ages (e.g., Faisst et al. 2017; Narayanan et al. 2018). These diagnostics suggest that HZ10 may resemble DSFGs with an elevated IR-to-UV luminosity ratio, intriguingly sharing similarities to lower-redshift IR-selected galaxies (e.g., Casey et al. 2014). However, HZ10 was selected through the LBG and LAE techniques at $z \sim 5.7$ and appears "typical" based on its UV emission. In particular, HZ10 lies within the scatter of the main sequence at this redshift (e.g., Speagle et al. 2014; Capak et al. 2015; Barišić et al. 2017; Faisst et al. 2017). Faisst et al. (2017) also interpreted the observed properties of LBG-1 as being consistent with lower dust and metal abundances, likely connected to young stellar populations. The IRX/$\beta_{\rm UV}$ diagnostic, however, would suggest that HZ4 and especially HZ9 may be more dusty than LBG-1, since they lie on or above the local Meurer et al. (1999) relation (Faisst et al. 2017). However, the measured [C II]/[N II] ratios for HZ4 and HZ9 are compatible with that in LBG-1 and significantly higher than the ratio in HZ10 (Figure 6). The intriguing finding of faint [N II] emission together with a relatively bright dust continuum in HZ9 therefore suggests the presence of additional variables controlling the relationship between the level of dust obscuration and the metallicity (or age of the most recent stellar population), which may be critical to diagnose the interplay between gas inflows, outflows, and star formation. An important next step would require measuring the CO line luminosity from HZ9, as well as achieving a detection in LBG-1. In case of relatively bright CO emission (e.g., in relation to its FIR luminosity) from HZ9, the high [C II]/[N II] line ratio would not be explained by the analogy to local dwarf galaxies and would point to previously unexplored star formation conditions. However, faint CO line emission from HZ9 would either suggest variations in the dust SED shape or intriguingly suggest the possibility of significant dust-obscured star formation even in more "typical," lower-metallicity, younger high-redshift galaxies. The ratio of our continuum measurements tentatively suggests higher dust temperatures in HZ9 than in HZ10. If correct, this might imply that the moderate IR luminosity in HZ9 may be due to higher temperatures, perhaps associated with higher radiation intensity, rather than a high dust content (Faisst et al. 2017). Béthermin et al. (2015) already presented evidence in favor of such rising radiation field intensity and dust temperatures toward higher redshift and showed that these may be a direct consequence of decreasing metallicity. Ferrara et al. (2017) suggested that galaxies at $z > 5$ may be FIR-faint due to colder dust than "normal" due to the very high molecular gas fraction. Their prediction of bright CO emission, specifically from galaxies with low IRX, may be in conflict with our deep upper limits on the CO luminosity from LBG-1. However, this effect may link the high molecular gas mass fraction in HZ10 to the tentatively lower dust temperature we observe in this galaxy relative to the rest of the sample (Ferrara et al. 2017).

The faint [N II] emission from HZ4 and HZ9, together with significant dust-obscured star formation, may be analogous to the properties observed in the eastern component of SPT 0311-58 (Marrone et al. 2018). This galaxy at $z = 6.90$ was shown to display high [O III] 88 μm luminosity ($\sim$2$\times$ its [C II] luminosity) while being characterized by very high dust-obscured star formation (at the level observed in HZ9 and HZ10). Similarly, the bright [O III] emitters studied by Hashimoto et al. (2019) and Tamura et al. (2019) at $z > 7$, which also show significant dust emission, may be somewhat analogous to the case we observe in HZ9, i.e., high intensity and hardness of the radiation causing a higher ionization state in the ionized ISM while showing significant dust-obscured star formation. Furthermore, a comparison of the [O III]/[C II] luminosity in two quasars at $z \sim 6$ suggests that this line ratio may strongly correlate with dust temperatures (Hashimoto et al. 2018a), supporting our interpretation of higher dust temperatures in [N II]-faint galaxies. We therefore suggest that a higher dust temperature may drive the observed FIR luminosity in such galaxies, perhaps due to a significant contribution from dust in the ionized regions (Faisst et al. 2017).

In order to assess how common the different star-forming conditions observed in LBG-1, HZ9, and HZ10 are, larger samples of "normal" galaxies at $z = 5$–6 need to be studied. The ALMA Large Program to Investigate [C II] at Early Times (ALPINE)[15] is now observing the [C II] and dust emission from large samples of typical galaxies at $4 < z < 6$ over a wide

[15] https://cesam.lam.fr/a2c2s/index.php

range of stellar mass and SFR. While the brightness of the [C II] and dust continuum, and their relation to the UV flux, provide a wealth of information (e.g., distinguishing LBG-1 from HZ10-type conditions), our analysis shows that relevant residual degrees of freedom are unconstrained unless either CO or a tracer of the ionized gas (such as [N II], [N III], or [O III]) is measured in addition to [C II] (to distinguish HZ10 from HZ9-type conditions), possibly due to metallicity and/or dust temperature variations. Furthermore, resolved observations for larger samples of galaxies are necessary because accurate dynamical masses may be the best way to constrain the gas mass and, hence, to directly infer the $\alpha_{\rm CO}$ conversion factor.

5. Conclusions

We have presented measurements of CO(2–1) line emission from two "normal" LBGs at the end of the "epoch of reionization," achieving the highest-redshift low-J CO detection from a main-sequence galaxy to date. We have found a large variation in the CO line luminosity between the two targeted sources that may not be completely accounted for by SFR differences (the CO luminosity ratio is $\gtrsim$6.5, while the SFR ratio is $\sim$3). While this difference in CO luminosity may suggest variations in star formation efficiency, it appears consistent with our expectation of lower gas metallicity and dust abundance strongly affecting the CO abundance. We infer a large molecular gas reservoir in at least one of the sources, suggesting low-efficiency star formation with gas depletion time $\sim$1 Gyr already at $z \sim 6$, analogous to what is commonly observed in lower-redshift disk galaxies. This low efficiency contrasts with what is typically observed in $z > 5$ starbursts and provides the first evidence of such "main-sequence" star-forming conditions at $z > 3$. We also find evidence for a continuously rising gas fraction up to $z \sim 6$, although our sample may suggest either significant scatter or systematic variations in the $\alpha_{\rm CO}$ conversion factor.

By observing the largest sample of "normal" galaxies at $z > 5$ in [N II] 205 μm emission to date, we find a general trend of increasing [C II]/[N II] ratios with lower IR luminosity, consistent with what was previously reported by Pavesi et al. (2016). Our findings support an interpretation where low gas and stellar metallicity raises the ionization state of carbon and nitrogen in the ionized gas. This interpretation suggests that the large majority of [C II] emission from most "normal" galaxies at $z > 5$ may emerge from the neutral gas phase. We also find a high [C II]/[N II] ratio in our sample with moderate IR luminosity, suggesting either significant dust temperature variations affecting the IR luminosity estimate or the possibility of a young starburst with high radiation intensity and hardness (and potentially low metallicity) together with substantial dust obscuration. Our findings imply that a significant fraction of main-sequence star formation taking place up to $z \sim 6$ may resemble the conditions observed in "normal" galaxies at lower redshift, suggesting that the efficiency of star formation may only weakly depend on those physical properties that are affected by redshift evolution. In particular, the high inferred gas fractions and higher merger rates do not appear to significantly affect main-sequence star formation. Although low metallicity may be common in the main-sequence galaxy population at $z > 5$, we do not find conclusive evidence for an effect on the star-forming conditions, although larger samples and more sensitive observations are needed to study this fainter population.

We thank Chelsea Sharon and Avani Gowardhan for useful discussion. R.P. and D.R. acknowledge support from the National Science Foundation under grant No. AST-1614213 to Cornell University. R.P. acknowledges support through award SOSPA3-008 from the NRAO. The National Radio Astronomy Observatory is a facility of the National Science Foundation operated under cooperative agreement by Associated Universities, Inc. This paper makes use of the following ALMA data: ADS/JAO. ALMA#2015.1.00928.S, 2015.1.00388.S, 2012.1.00523.S, 2011.0.00064.S. ALMA is a partnership of the ESO (representing its member states), NSF (USA), and NINS (Japan), together with the NRC (Canada), NSC and ASIAA (Taiwan), and KASI (Republic of Korea), in cooperation with the Republic of Chile. The Joint ALMA Observatory is operated by the ESO, AUI/NRAO, and NAOJ.

Appendix A
SED

Here we present the results of modified blackbody fitting to the available dust continuum observations in the full galaxy sample. The limited sampling of the dust emission is responsible for the high uncertainties on the predicted FIR peak. We illustrate the results of our probabilistic analysis with a gradient of color shading, derived using the results of the MCMC samples, showing the fitting results and higher confidence regions in darker shading (Figure 7). We also present best-fit stellar emission models to the archival optical and NIR observations as templates, previously described by Capak et al. (2015).

Appendix B
Dynamical Modeling

We have carried out a dynamical modeling analysis directly on the visibilities for the [C II] observations in HZ9 and HZ10 using `GALARIO` (Tazzari et al. 2018) and `Multinest` (Feroz et al. 2009), using the method[16] previously described by Pavesi et al. (2018a). While the [C II] line in HZ9 and HZ10 shows a smooth velocity gradient, the line in LBG-1 shows a more complex morphology and dynamics, with three components and two separate velocity gradients (Riechers et al. 2014). Therefore, we do not attempt to model the emission from LBG-1, as the data are not sufficient to properly constrain such a high-complexity model. Although the [C II] line in HZ10 shows a smooth velocity gradient, the *Hubble Space Telescope* NIR and dust continuum images from ALMA suggest the presence of two separate morphological components. These may be associated with either a galaxy merger or clumpy gas and stellar distributions embedded in a rotating disk. The somewhat asymmetric [C II] line profile may also be caused by massive gas clumps, as shown by the simulations of Daddi et al. (2010a) and Bournaud et al. (2014, 2015).

We simultaneously fit a rotating disk model generated by KinMS (Davis et al. 2013) to the line emission and a simple continuum model (one and two Gaussian components for HZ9 and HZ10, respectively). We model the line emission intensity as a Gaussian profile and the rotation curve as a "tangent" function parameterized by the maximum velocity and half-maximum radius (Table 3). We fit a total of 18 parameters for HZ10 (also including line flux, disk center along each coordinate, and continuum sizes, fluxes, and position for both

[16] Python code available at https://github.com/pavesiriccardo/UVmodeldisk.

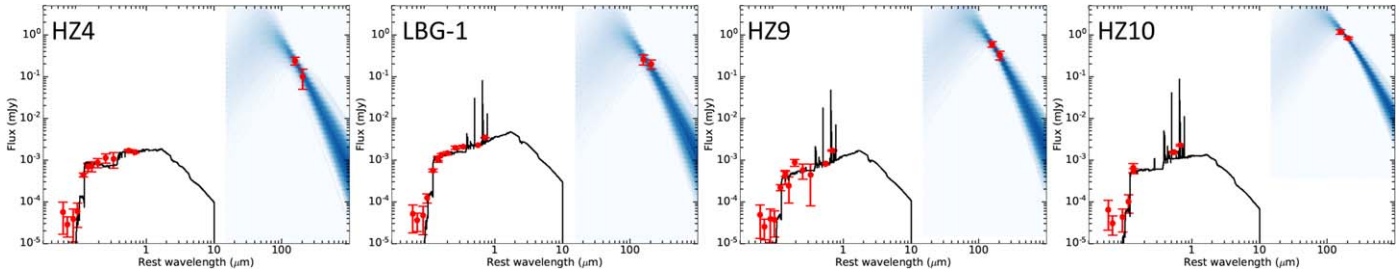

Figure 7. Optical-to-FIR SED for the full galaxy sample. Observed optical-to-NIR (from the catalog presented by Laigle et al. 2016) and FIR fluxes presented here are shown as red circles. Optical-to-NIR fitting to the stellar emission is shown in black (Capak et al. 2015). Modified blackbody fitting to the FIR emission described in the text is shown as blue shading, with darker shading indicating higher-probability areas.

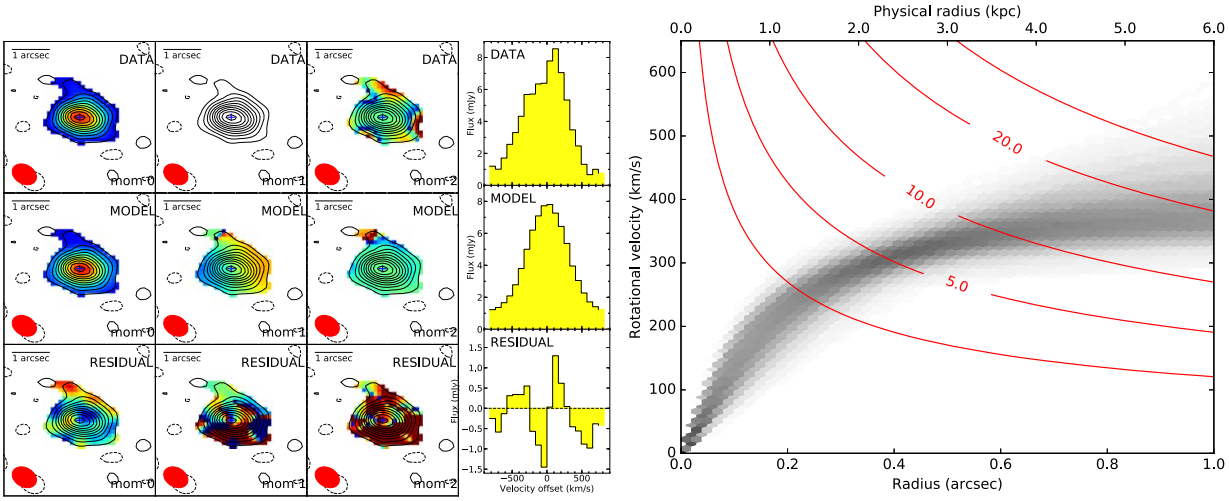

Figure 8. Left: visibility space dynamical modeling results for the [C II] line emission in HZ10. We show the "natural" weighting line moment zero (intensity), 1 (velocity), and 2 (dispersion) maps and spectra for the data, the single-disk model corresponding to posterior median parameters, and the visibility residuals. Two Gaussian components were adopted as models for the continuum. Right: probabilistic constraints to the rotation curve for a "tan" model with two disk modeling parameters (maximum velocity and half-velocity radius). The darker shading corresponds to higher probability density, as determined by the MCMC samples. We also show the enclosed dynamical mass in units of $10^{10}\,M_{\odot}$ (red curves).

Table 3
Results of Dynamical Modeling for Our Sample Galaxies

	HZ10			HZ9		
Parameter (Units)	16th perc.	50th perc.	84th perc.	16th perc.	50th perc.	84th perc.
Gas dispersion (km s^{-1})	210	218	226	80	89	100
Emission FWHM (arcsec)	0.84	0.88	0.91	0.47	0.51	0.55
Maximum velocity (km s^{-1})	380	430	510	300	445	750
Velocity scale length (arcsec)	0.12	0.18	0.28	0.014	0.03	0.08
Inclination (deg)	59	61	63	13	21	31
Position angle (deg)	−7	−5	−3	71	77	83

components) and 12 parameters for HZ9 (also including line flux, disk center along each coordinate, and continuum size and flux) as afforded by the available signal-to-noise ratio. The data, median-parameter model (indistinguishable from the best-fit model), and residuals are shown in Figures 8 and 9, together with the derived probabilistic constraints to the rotation curve as a function of radius and the implied dynamical masses enclosed within that radius.

Because of the limitation of assuming a single-disk model, we note that substantial uncertainties regarding the detailed dynamics of HZ10 affect our inference, as evidenced by the nonnegligible residual structure after model fitting. We use the disk model scale length and rotation curve to derive dynamical mass estimates within the half-light radius by adopting the measured rotational velocity. We do not apply corrections for velocity dispersion because the physical origin of the apparent dispersion is uncertain (particularly in the case of HZ10, for which two distinct components may be partly responsible for the line broadening). We estimate that these systematic corrections may be as large as ∼50%, toward increasing the dynamical masses inferred by fitting a rotating disk, based on the measured gas dispersion ($\sigma \sim 90 \pm 10$ and $220 \pm 10\,\mathrm{km\,s^{-1}}$ for HZ9 and HZ10, respectively). We obtain $\sim(6.1 \pm 0.7) \times 10^{10}\,M_{\odot}$ for HZ10 and only an approximate estimate of $5^{+5}_{-3} \times 10^{10}\,M_{\odot}$ for HZ9, within the half-light radius of the [C II] emission. Our results agree within the uncertainties

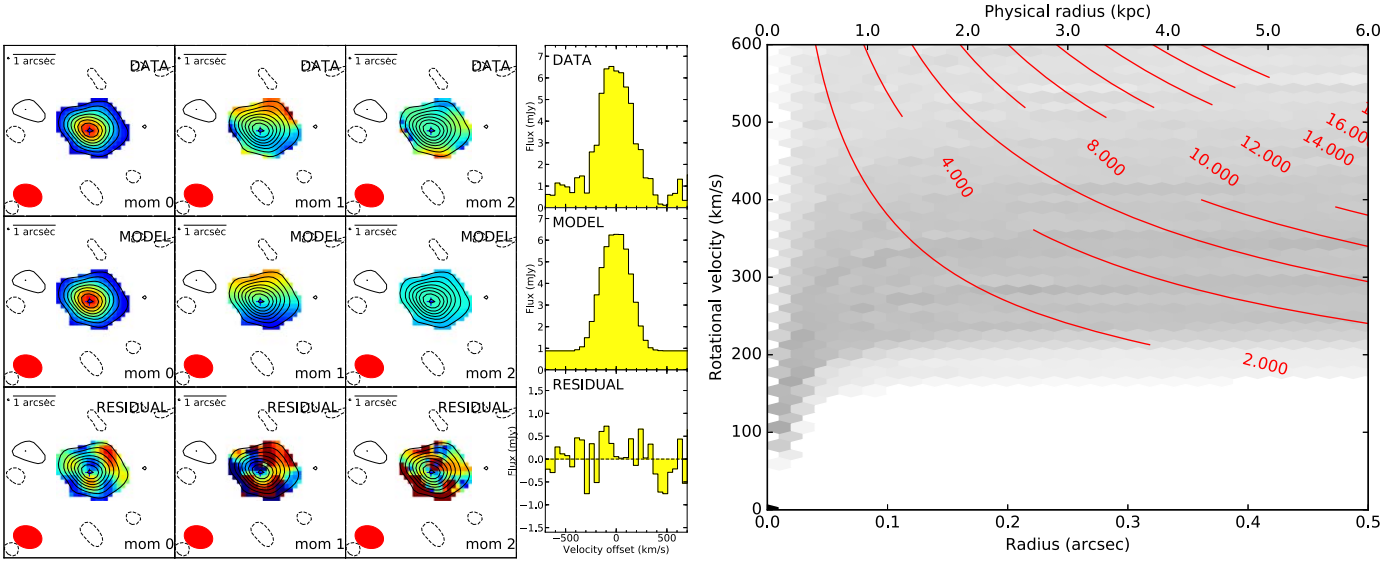

Figure 9. Dynamical modeling results for HZ9. A single Gaussian component was adopted as a continuum model. See Figure 8 for further details.

with previous estimates based on tilted-ring modeling in the image plane by Jones et al. (2017), although our uncertainty estimates are significantly more conservative due to the larger number of fitted parameters.

ORCID iDs

Riccardo Pavesi https://orcid.org/0000-0002-2263-646X
Dominik A. Riechers https://orcid.org/0000-0001-9585-1462
Andreas L. Faisst https://orcid.org/0000-0002-9382-9832
Peter L. Capak https://orcid.org/0000-0003-3578-6843

References

Barišić, I., Faisst, A. L., Capak, P. L., et al. 2017, ApJ, 845, 41
Behroozi, P., Wechsler, R., Hearin, A., & Conroy, C. 2019, MNRAS, 488, 3143
Béthermin, M., Daddi, E., Magdis, G., et al. 2015, A&A, 573, A113
Béthermin, M., De Breuck, C., Gullberg, B., et al. 2016, A&A, 586, L7
Bigiel, F., Leroy, A., Walter, F., et al. 2008, AJ, 136, 2846
Bigiel, F., Leroy, A. K., Walter, F., et al. 2011, ApJL, 730, L13
Bolatto, A. D., Wolfire, M., & Leroy, A. K. 2013, ARA&A, 51, 207
Bothwell, M. S., Chapman, S. C., Tacconi, L., et al. 2010, MNRAS, 405, 219
Bouché, N., Cresci, G., Davies, R., et al. 2007, ApJ, 671, 303
Bournaud, F., Daddi, E., Weiß, A., et al. 2015, A&A, 575, A56
Bournaud, F., Perret, V., Renaud, F., et al. 2014, ApJ, 780, 57
Bourne, N., Dunne, L., Bendo, G. J., et al. 2013, MNRAS, 436, 479
Bouwens, R. J., Aravena, M., Decarli, R., et al. 2016, ApJ, 833, 72
Bouwens, R. J., Illingworth, G. D., Oesch, P. A., et al. 2015, ApJ, 803, 34
Buckley, M. R., & Peter, A. H. G. 2018, PhR, 761, 1
Calistro Rivera, G., Hodge, J. A., Smail, I., et al. 2018, ApJ, 863, 56
Capak, P. L., Carilli, C., Jones, G., et al. 2015, Natur, 522, 455
Carilli, C. L., Riechers, D., Walter, F., et al. 2013, ApJ, 763, 120
Carilli, C. L., & Walter, F. 2013, ARA&A, 51, 105
Carniani, S., Maiolino, R., Pallottini, A., et al. 2017, A&A, 605, A42
Casey, C. M. 2012, MNRAS, 425, 3094
Casey, C. M., Scoville, N. Z., Sanders, D. B., et al. 2014, ApJ, 796, 95
Castellano, M., Pentericci, L., Vanzella, E., et al. 2018, ApJL, 863, L3
Chiang, Y.-K., Overzier, R. A., Gebhardt, K., & Henriques, B. 2017, ApJL, 844, L23
Combes, F., Rex, M., Rawle, T. D., et al. 2012, A&A, 538, L4
Coppin, K. E. K., Swinbank, A. M., Neri, R., et al. 2007, ApJ, 665, 936
Cormier, D., Madden, S. C., Lebouteiller, V., et al. 2014, A&A, 564, A121
Cormier, D., Madden, S. C., Lebouteiller, V., et al. 2015, A&A, 578, A53
Croxall, K. V., Smith, J. D., Pellegrini, E., et al. 2017, ApJ, 845, 96
da Cunha, E., Groves, B., Walter, F., et al. 2013, ApJ, 766, 13
Daddi, E., Bournaud, F., Walter, F., et al. 2010a, ApJ, 713, 686
Daddi, E., Dannerbauer, H., Liu, D., et al. 2015, A&A, 577, A46
Daddi, E., Elbaz, D., Walter, F., et al. 2010b, ApJL, 714, L118
Davé, R., Finlator, K., & Oppenheimer, B. D. 2011, MNRAS, 416, 1354
Davé, R., Finlator, K., & Oppenheimer, B. D. 2012, MNRAS, 421, 98
Davis, T. A., Alatalo, K., Bureau, M., et al. 2013, MNRAS, 429, 534
De Breuck, C., Williams, R. J., Swinbank, M., et al. 2014, A&A, 565, A59
Decarli, R., Walter, F., Aravena, M., et al. 2016, ApJ, 833, 70
Decarli, R., Walter, F., Carilli, C., et al. 2014, ApJL, 782, L17
Decarli, R., Walter, F., Venemans, B. P., et al. 2017, Natur, 545, 457
Dessauges-Zavadsky, M., Zamojski, M., Rujopakarn, W., et al. 2017, A&A, 605, A81
Dessauges-Zavadsky, M., Zamojski, M., Schaerer, D., et al. 2015, A&A, 577, A50
Díaz-Santos, T., Armus, L., Charmandaris, V., et al. 2013, ApJ, 774, 68
Díaz-Santos, T., Armus, L., Charmandaris, V., et al. 2017, ApJ, 846, 32
Eales, S., Smith, M. W. L., Auld, R., et al. 2012, ApJ, 761, 168
Engel, H., Tacconi, L. J., Davies, R. I., et al. 2010, ApJ, 724, 233
Faisst, A. L., Capak, P., Hsieh, B. C., et al. 2016a, ApJ, 821, 122
Faisst, A. L., Capak, P. L., Davidzon, I., et al. 2016b, ApJ, 822, 29
Faisst, A. L., Capak, P. L., Yan, L., et al. 2017, ApJ, 847, 21
Farrah, D., Lebouteiller, V., Spoon, H. W. W., et al. 2013, ApJ, 776, 38
Feroz, F., Hobson, M. P., & Bridges, M. 2009, MNRAS, 398, 1601
Ferrara, A. 2016, ASSL, 423, 163
Ferrara, A., Hirashita, H., Ouchi, M., & Fujimoto, S. 2017, MNRAS, 471, 5018
Förster Schreiber, N. M., Genzel, R., Bouché, N., et al. 2009, ApJ, 706, 1364
Geach, J. E., Smail, I., Moran, S. M., et al. 2011, ApJL, 730, L19
Genzel, R., Tacconi, L. J., Combes, F., et al. 2012, ApJ, 746, 69
Genzel, R., Tacconi, L. J., Gracia-Carpio, J., et al. 2010, MNRAS, 407, 2091
Genzel, R., Tacconi, L. J., Lutz, D., et al. 2015, ApJ, 800, 20
Gowardhan, A., Riechers, D., Pavesi, R., et al. 2019, ApJ, 875, 6
Gowardhan, A., Riechers, D. A., Daddi, E., et al. 2017, ApJ, 838, 136
Groves, B. A., Schinnerer, E., Leroy, A., et al. 2015, ApJ, 799, 96
Gullberg, B., De Breuck, C., Vieira, J. D., et al. 2015, MNRAS, 449, 2883
Harikane, Y., Ouchi, M., Shibuya, T., et al. 2018, ApJ, 859, 84
Hashimoto, T., Inoue, A. K., Mawatari, K., et al. 2019, PASJ, 71, 71
Hashimoto, T., Inoue, A. K., Tamura, Y., et al. 2018a, arXiv:1811.00030
Hashimoto, T., Laporte, N., Mawatari, K., et al. 2018b, Natur, 557, 392
Herrera-Camus, R., Bolatto, A., Smith, J. D., et al. 2016, ApJ, 826, 175
Hildebrand, R. H. 1983, QJRAS, 24, 267
Hodge, J. A., Swinbank, A. M., Simpson, J. M., et al. 2016, ApJ, 833, 103
Hollenbach, D. J., & Tielens, A. G. G. M. 1997, ARA&A, 35, 179
Hopkins, P. F., Kereš, D., Oñorbe, J., et al. 2014, MNRAS, 445, 581
Inoue, A. K., Tamura, Y., Matsuo, H., et al. 2016, Sci, 352, 1559
Jameson, K. E., Bolatto, A. D., Wolfire, M., et al. 2018, ApJ, 853, 111
Jones, G. C., Carilli, C. L., Shao, Y., et al. 2017, ApJ, 850, 180
Kaufman, M. J., Wolfire, M. G., Hollenbach, D. J., & Luhman, M. L. 1999, ApJ, 527, 795
Kennicutt, R. C., & Evans, N. J. 2012, ARA&A, 50, 531
Kennicutt, R. C., Jr. 1998, ApJ, 498, 541

Krumholz, M. R., Burkhart, B., Forbes, J. C., & Crocker, R. M. 2018, MNRAS, 477, 2716
Laigle, C., McCracken, H. J., Ilbert, O., et al. 2016, ApJS, 224, 24
Laporte, N., Ellis, R. S., Boone, F., et al. 2017, ApJL, 837, L21
Leroy, A. K., Bolatto, A., Gordon, K., et al. 2011, ApJ, 737, 12
Leroy, A. K., Walter, F., Bigiel, F., et al. 2009, AJ, 137, 4670
Leroy, A. K., Walter, F., Brinks, E., et al. 2008, AJ, 136, 2782
Leroy, A. K., Walter, F., Sandstrom, K., et al. 2013, AJ, 146, 19
Liang, L., Feldmann, R., Faucher-Giguère, C.-A., et al. 2018, MNRAS, 478, L83
Lilly, S. J., Carollo, C. M., Pipino, A., Renzini, A., & Peng, Y. 2013, ApJ, 772, 119
Litke, K. C., Marrone, D. P., Spilker, J. S., et al. 2019, ApJ, 870, 80
Lu, N., Cao, T., Díaz-Santos, T., et al. 2018, ApJ, 864, 38
Luhman, M. L., Satyapal, S., Fischer, J., et al. 1998, ApJL, 504, L11
Ma, X., Hopkins, P. F., Garrison-Kimmel, S., et al. 2018, MNRAS, 478, 1694
Madden, S. C., Poglitsch, A., Geis, N., Stacey, G. J., & Townes, C. H. 1997, ApJ, 483, 200
Magdis, G. E., Daddi, E., Béthermin, M., et al. 2012, ApJ, 760, 6
Magdis, G. E., Daddi, E., Elbaz, D., et al. 2011, ApJL, 740, L15
Magnelli, B., Saintonge, A., Lutz, D., et al. 2012, A&A, 548, A22
Maiolino, R., Caselli, P., Nagao, T., et al. 2009, A&A, 500, L1
Maiolino, R., Cox, P., Caselli, P., et al. 2005, A&A, 440, L51
Malhotra, S., Kaufman, M. J., Hollenbach, D., et al. 2001, ApJ, 561, 766
Maloney, P., & Black, J. H. 1988, ApJ, 325, 389
Marrone, D. P., Spilker, J. S., Hayward, C. C., et al. 2018, Natur, 553, 51
Masters, D., Faisst, A., & Capak, P. 2016, ApJ, 828, 18
Meurer, G. R., Heckman, T. M., & Calzetti, D. 1999, ApJ, 521, 64
Moster, B. P., Naab, T., & White, S. D. M. 2018, MNRAS, 477, 1822
Nagao, T., Maiolino, R., De Breuck, C., et al. 2012, A&A, 542, L34
Nagao, T., Maiolino, R., Marconi, A., & Matsuhara, H. 2011, A&A, 526, A149
Narayanan, D., Davé, R., Johnson, B. D., et al. 2018, MNRAS, 474, 1718
Oberst, T. E., Parshley, S. C., Stacey, G. J., et al. 2006, ApJL, 652, L125
Orr, M. E., Hayward, C. C., Hopkins, P. F., et al. 2018, MNRAS, 478, 3653
Oteo, I., Ivison, R. J., Dunne, L., et al. 2016, ApJ, 827, 34
Pavesi, R., Riechers, D. A., Capak, P. L., et al. 2016, ApJ, 832, 151
Pavesi, R., Riechers, D. A., Sharon, C. E., et al. 2018a, ApJ, 861, 43
Pavesi, R., Sharon, C. E., Riechers, D. A., et al. 2018b, ApJ, 864, 49
Privon, G. C., Narayanan, D., & Davé, R. 2018, ApJ, 867, 102
Rawle, T. D., Egami, E., Bussmann, R. S., et al. 2014, ApJ, 783, 59
Reddy, N. A., Erb, D. K., Pettini, M., Steidel, C. C., & Shapley, A. E. 2010, ApJ, 712, 1070
Reddy, N. A., Oesch, P. A., Bouwens, R. J., et al. 2018, ApJ, 853, 56
Reddy, N. A., Steidel, C. C., Fadda, D., et al. 2006, ApJ, 644, 792
Riechers, D. A., Bradford, C. M., Clements, D. L., et al. 2013, Natur, 496, 329
Riechers, D. A., Capak, P. L., Carilli, C. L., et al. 2010a, ApJL, 720, L131
Riechers, D. A., Carilli, C. L., Capak, P. L., et al. 2014, ApJ, 796, 84
Riechers, D. A., Carilli, C. L., Walter, F., & Momjian, E. 2010b, ApJL, 724, L153
Riechers, D. A., Pavesi, R., Sharon, C. E., et al. 2019, ApJ, 872, 7
Sandstrom, K. M., Leroy, A. K., Walter, F., et al. 2013, ApJ, 777, 5
Schruba, A., Leroy, A. K., Walter, F., et al. 2011, AJ, 142, 37
Scoville, N., Arnouts, S., Aussel, H., et al. 2013, ApJS, 206, 3
Scoville, N., Lee, N., Vanden Bout, P., et al. 2017, ApJ, 837, 150
Scoville, N., Sheth, K., Aussel, H., et al. 2016, ApJ, 820, 83
Scoville, N. Z. 2013, in Evolution of Star Formation and Gas, ed. J. Falcón-Barroso & J. H. Knapen (Cambridge: Cambridge Univ. Press), 491
Sharda, P., Federrath, C., da Cunha, E., Swinbank, A. M., & Dye, S. 2018, MNRAS, 477, 4380
Silverman, J. D., Daddi, E., Rodighiero, G., et al. 2015, ApJL, 812, L23
Silverman, J. D., Rujopakarn, W., Daddi, E., et al. 2018, ApJ, 867, 92
Smith, J. D. T., Croxall, K., Draine, B., et al. 2017, ApJ, 834, 5
Speagle, J. S., Steinhardt, C. L., Capak, P. L., & Silverman, J. D. 2014, ApJS, 214, 15
Spilker, J. S., Bezanson, R., Marrone, D. P., et al. 2016, ApJ, 832, 19
Stacey, G. J., Geis, N., Genzel, R., et al. 1991, ApJ, 373, 423
Stacey, G. J., Hailey-Dunsheath, S., Ferkinhoff, C., et al. 2010, ApJ, 724, 957
Steinhardt, C. L., Speagle, J. S., Capak, P., et al. 2014, ApJL, 791, L25
Strandet, M. L., Weiss, A., De Breuck, C., et al. 2017, ApJL, 842, L15
Strom, A. L., Steidel, C. C., Rudie, G. C., et al. 2017, ApJ, 836, 164
Strom, A. L., Steidel, C. C., Rudie, G. C., Trainor, R. F., & Pettini, M. 2018, ApJ, 868, 117
Tacchella, S., Bose, S., Conroy, C., Eisenstein, D. J., & Johnson, B. D. 2018, ApJ, 868, 92
Tacconi, L. J., Genzel, R., Saintonge, A., et al. 2018, ApJ, 853, 179
Tacconi, L. J., Genzel, R., Smail, I., et al. 2008, ApJ, 680, 246
Tacconi, L. J., Neri, R., Genzel, R., et al. 2013, ApJ, 768, 74
Tamura, Y., Mawatari, K., Hashimoto, T., et al. 2019, ApJ, 874, 27
Tan, Q., Daddi, E., Magdis, G., et al. 2014, A&A, 569, A98
Tan, Q., Daddi, E., Sargent, M., et al. 2013, ApJL, 776, L24
Tazzari, M., Beaujean, F., & Testi, L. 2018, MNRAS, 476, 4527
Tremonti, C. A., Heckman, T. M., Kauffmann, G., et al. 2004, ApJ, 613, 898
Umehata, H., Matsuda, Y., Tamura, Y., et al. 2017, ApJL, 834, L16
Vallini, L., Pallottini, A., Ferrara, A., et al. 2018, MNRAS, 473, 271
Venemans, B. P., Walter, F., Zschaechner, L., et al. 2016, ApJ, 816, 37
Vincenzo, F., Belfiore, F., Maiolino, R., Matteucci, F., & Ventura, P. 2016, MNRAS, 458, 3466
Wagg, J., Carilli, C. L., Wilner, D. J., et al. 2010, A&A, 519, L1
Walter, F., Decarli, R., Carilli, C., et al. 2012, Natur, 486, 233
Walter, F., Riechers, D., Cox, P., et al. 2009, Natur, 457, 699
Wolfire, M. G., Hollenbach, D., & Tielens, A. G. G. M. 1989, ApJ, 344, 770
Wolfire, M. G., Tielens, A. G. G. M., & Hollenbach, D. 1990, ApJ, 358, 116
Zavala, J. A., Montaña, A., Hughes, D. H., et al. 2018, NatAs, 2, 56
Zhao, Y., Lu, N., Xu, C. K., et al. 2016, ApJ, 819, 69